Method of Characteristics for transient, planar, cylindrical flows

Alan E. Vardy[a,*], Sjoerd W. Rienstra[b], Honglin Wang[c]

[a]*School of Science and Engineering, University of Dundee, Dundee, DD1 4HN, United Kingdom*
[b]*Department of Mathematics and Computer Science, Eindhoven University of Technology, P.O.Box 513, Eindhoven, 5600 MB, The Netherlands*
[c]*School of Mechanical Engineering, Southwest Jiaotong University, Sichuan, China*

Abstract

Cylindrical radiation of individual pulses is studied and strong differences from spherical radiation are highlighted. Prior to this study, the class of available analytical solutions for cylindrical radiation was rather limited. It included (i) a well-known solution for a steady-state, time-harmonic line source and (ii) the solution for a delta-pulse line source. The first of these has no analytical counterpart for individual pulses. By means of the second (actually the Green's function) a more general class of line source solutions can be formulated, but each one is in the form of an integral that has to be evaluated numerically and requires tedious preparation of a singular integrand, making it difficult to achieve perfect accuracy. In the present paper, use is made instead of a particular family of analytically-exact (linear) solutions that has been developed recently. It is used to assess the accuracy of solutions obtained numerically by the method of characteristics (MoC), which is then applied to more general sources than those amenable to analytical treatment. The MoC analysis is specially formulated to reduce the influence of terms involving the reciprocal of the radius (such terms are numerically unmanageable close to the origin). It is found that the qualitative behaviour of waves radiating from the surface of a cylinder of finite radius can depend strongly on the duration of the initiating disturbance and that this can be interpreted in a convolution-like manner. After validation, the numerical method is coupled with a conventional MoC analysis of planar wave propagation and is used to simulate the reflection and radiation of an initially planar wavefront arriving at a flanged duct exit. The

*Corresponding author
Email address: a.e.vardy@dundee.ac.uk (Alan E. Vardy)

numerical representation is one-dimensional in both domains – (x, t) inside the duct and (r, t) outside it. Although its use implies identical behaviour in all radial directions in the external domain, the solution is found to be in close agreement with circumferential-average values from a CFD solution that simulates azimuthal variations as well as radial variations. Whilst being less comprehensive than the CFD simulation, the MoC analysis has the important practical benefit of making highly efficient use of human and computational resources. By comparing the MoC and CFD solutions, it is found that the nominally-cylindrical radiation from the duct approximates closely to radiation from a line source a small distance inside the duct (not at the exit plane). An approximate location of the effective source is quantified.

Keywords: cylindrically-symmetric flow, wave radiation, wave reflection, method of characteristics, vibrating cylinder acoustics, tunnel portals.

List of symbols

1D	spatially one-dimensional
2D	spatially two-dimensional
a	radius of cylinder (or sphere) [m]
A	small non-dimensional amplitude to warrant linearisation (here $A = 2\pi \cdot 10^{-3}$)
b	pulse duration; reference time [s]
B_n	B(ulge)-shaped source function
C	source term in Eq. (3) [kg/m^2 s]
c	sound speed [m/s]
c_0	ambient sound speed [m/s]
cosh	hyperbolic cosine
acosh	inverse hyperbolic cosine
d	diameter of circular-section duct [m]
f_n	$= H(t)t^n$, elementary source function
$g(t)$	generic polynomial in t
$\tilde{g}(t-1)$	functionally equal to $g(t)$, but written as polynomial in $t-1$
H	height of slot or rectangular-section duct [m]
$H(t)$	Heaviside unit step-function (nondimensional, irrespective of argument)
M	source term in Eq. (4) [kg/m s^2]
MoC	Method of Characteristics
$\dot{m}$	mass flowrate per unit length of line source [kg/m s]
n	integer (parameter of source shape functions)
N_n	N-shaped source function
p	pressure (dimensional [Pa], and nondimensional)
p_0	ambient pressure (dimensional [Pa])
q	source shape function (dimensional [Pa], and nondimensional)
r	radial coordinate (dimensional [m], and nondimensional)
R	radius of cylinder; half height of slot [m]
t	time coordinate (dimensional [s], and nondimensional)
u_r, v	radial velocity (dimensional [m/s], and nondimensional)
$\boldsymbol{v}$	vectorial velocity [m/s]
W	width of duct [m]
x	axial coordinate along uniform duct [m]
$\boldsymbol{x}$	2D position coordinate (dimensional [m], and nondimensional)
z	coordinate parallel to cylinder axis [m]

Greek characters

$\delta(\boldsymbol{x})$	delta-function (dimension is reciprocal of dimension of argument)
γ	ratio of principal specific heat capacities (nondimensional)
ζ	$= c_0 t / r$ (nondimensional)
φ	angle subtended at duct exit by borders of the outer domain
Φ	dimensionless mass flowrate per unit length
θ	azimuthal angle
ρ	density (dimensional [kg/m^3], and nondimensional)
ρ_0	ambient density [kg/m^3]

suffices

0	initial, ambient conditions
A, L, R	locations in (r, t) space
a	innermost radius of external flow domain (*i.e.* cylinder surface)

1. Introduction

Cylindrical wave propagation from line sources has received much less attention in the literature than spherical propagation from point sources. This is largely because of their relative rarity in practical instances, but it is also because equations describing cylindrical radiation are less amenable to simple mathematical analysis than their spherical counterparts. Indeed, in general, radiation in even numbers of spatial dimensions (2,4,6,...) is more complex than that in odd-numbers (1,3,5,...) – *e.g.* Balazs [1] – where 'dimensions' should be interpreted in a Cartesian sense (x, y, z). Likewise, following convention, the abbreviations 1D, 2D and 3D are used in this way wherever they appear even though extensive use is made of cylindrical coordinates in the mathematical derivations.

One purpose of this paper is to present and validate a numerical method of simulating cylindrical wave propagation with no azimuthal or axial component – *i.e.* (r, t) only, not (r, θ, t) or (r, z, t). The method, which is developed in Section 2, is formulated in a manner that reduces the numerical influence of terms involving the reciprocal of the radius. Another purpose is to increase understanding of cylindrical propagation of non-harmonic pulses, highlighting differences from spherical radiation. This is one focus of Section 3, in which comparisons are made with a new analytical method developed by Rienstra [2]. The analytical method is restricted to a particular class of cylindrically-symmetric cases, but that is sufficient for its use herein because it enables a rigorous assessment of the

new numerical implementation. This is done for a selection of cases in which a prescribed mass flowrate at the origin ($r = 0$) exists for only a finite duration, thereby causing a nominally isolated pulse to radiate outwards.

In principle, after validation, the numerical method could be used to investigate a wide range of pulse types that cannot be simulated analytically. That capability could be a significant benefit in practical applications where a need exists to study pulses generated in a range of operating conditions of particular systems. However, simply studying alternative pulse types would add little in the context of the present paper. Instead, a much more powerful use of the method is presented in Section 4 in which an interactive boundary condition is used to couple the numerical analysis with a nominally independent analysis. Specifically, the cylindrical analysis (r, t) is coupled directly with an analysis of uniaxial (x, t) wave propagation and is used to explore the behaviour of pressure waves in ducts when they reflect and radiate at the duct exit. This is a classical application, but it has traditionally been analysed only for less constrained external geometry that may be characterised loosely as allowing spherical-like radiation. The number of cases of more-constrained, cylindrical-like radiation from ducts is tiny in comparison with that of spherical-like radiation, but one instance of it was a key motivation for the present study. This was a need to know how pressure waves behave when radiating from railway tunnels emerging into narrow cuttings. Such situations are becoming increasingly common when environmental and other reasons force railways to be underground, especially in large urban areas.

Figure 1 gives schematic illustrations of the various cases considered. In the analytical method, waves radiate outwards from a line-source discontinuity at the origin (Fig. 1a). This is the geometry to which Rienstra's analytical method applies [2] and the solutions are valid for all radii from zero to infinity. The numerical method also assumes purely cylindrical radiation, but practical uses of it are restricted to finite inner and outer radii. The inner limit is necessarily finite because the numerical algorithms are incapable of handling discontinuities. However, this lower limit is further constrained by a practical need to use finite grid lengths whilst also ensuring that proportional changes in radius within any grid length do not cause unacceptable errors. Accordingly the inner boundary depicted in Fig. 1b is at a finite radius. The need for a finite outer limit of the calculation domain arises because of practical size limitations of computer memory. However, it is of little consequence herein because the boundary is chosen at a radius at which the flow remains undisturbed throughout the simulations. This geometry is suitable for studying, say, radial propagation from a source between parallel plates, or radiation from the surface of a long cylinder vibrating radially in

an identical manner (including in-phase) at all locations along its axis. Figures 1c and 1d show cases where the radiation is not purely radial. They are used in Section 4, which gives details of the above-mentioned study of radiation from a duct exit.

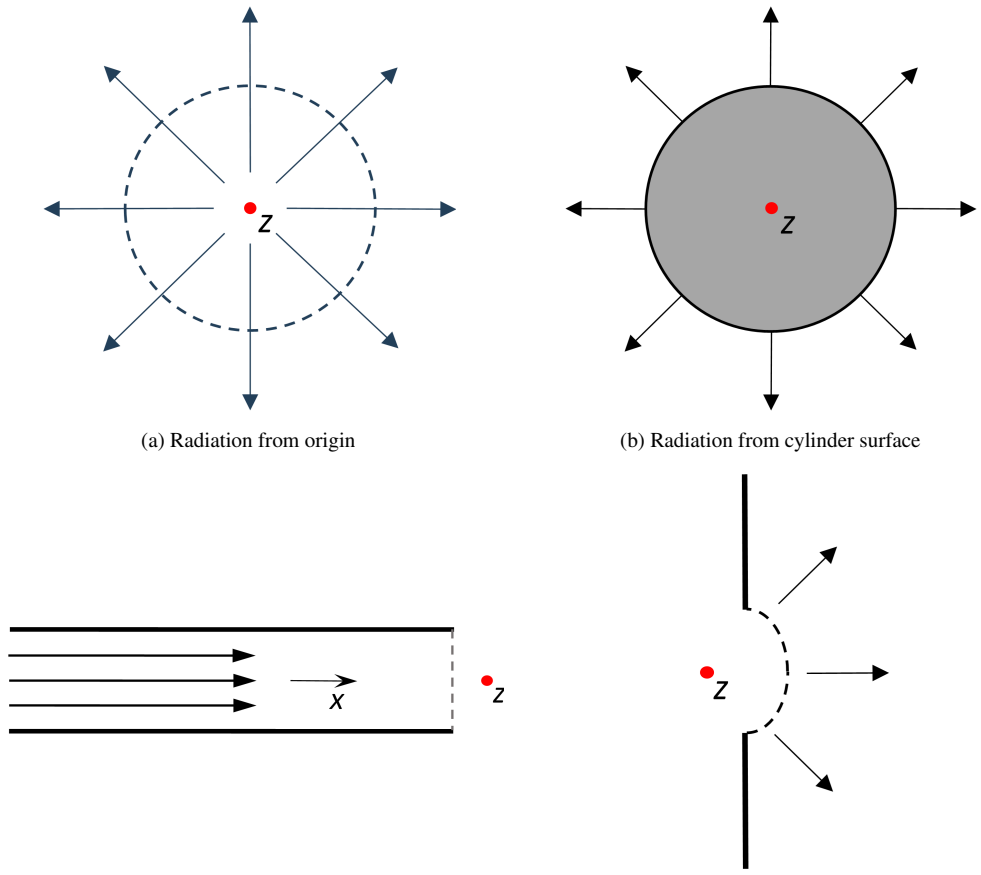

(a) Radiation from origin

(b) Radiation from cylinder surface

(c) Wave approaching a duct exit

(d) Radiation from the duct exit

Figure 1: Examples of 1D wave propagation – uniaxial and radial

1.1. Axial, spherical and cylindrical radiation

It is useful to precede the general discussion with a brief summary of differences between axial, spherical and cylindrical wave propagation. Consider, for instance, a continuous pressure pulse source (p, t) of arbitrary shape, but finite duration, propagating isentropically into a zone of initially-uniform ambient conditions. Further, for simplicity, temporarily restrict consideration to pulses of

small amplitude. Then, in the case of axial propagation along a uniform duct, the pressure history at any location will be almost identical to that at the source except for a time delay due to the finite speed of propagation of the pulse. Analogous behaviour also exists for spherical propagation except that the amplitude of the radiating pulse decreases with increasing radius. In both cases, no change occurs in either the shape or the duration of the propagating pulse, and ambient conditions prevail everywhere behind it. A very different result is found for cylindrically radiating pulses. For this, both the shape and the duration vary with the radial distance of travel. Indeed, at any location, the pressure never returns exactly to the ambient value, but instead approaches it asymptotically. This behaviour is quantified in Section 3 for purely cylindrical radiation and is illustrated in Figures presented therein. Subsequently, it is shown in Section 4 to have a strong influence on the reflection of waves from duct exits.

1.2. Analytical methods

Although the general behaviour of (linear) waves radiating cylindrically is understood – *e.g.* Lamb [3] – it has been less-widely studied than uniaxial or spherical propagation. Its dispersive behaviour renders it much less amenable to analytical treatment than its uniaxial and spherical counterparts. Analytical representations of it are rare and, before the authors began their study, none were found that seemed suitable for the proposed study. There is a well-known solution for a steady-state, time-harmonic line source in terms of a Hankel function – *e.g.* Jones [4, Ch.1.36] – and the Green's function for a delta-pulse source – Bleistein [5, Ch.5.3], Rienstra & Hirschberg [6, App.E]. By means of the latter, a more general class of line source solutions can be formulated – Lamb [3, Art.302] – but it is in the form of an integral that has to be evaluated numerically. This has practical disadvantages, due to the singular behaviour at the origin, when looking for simple and exact solutions to verify and test the accuracy of comprehensive numerical solutions such as the one developed herein.

In the case of a steady-state, time-harmonic line source, the pressure amplitude in the far field varies as the inverse square root of the radial coordinate, but it does not necessarily follow that the same is true for pulses in the time domain. However, starting from the Green's function in the time domain (and using essentially the same formulation as given by Lamb [3, Art.302]), Whitham [7, Ch.7.4 p.219-224] and Lighthill [8, Ch.1.4 p.21] analyse the general time-domain solution asymptotically for large time near and away from a pulse front. For a sinusoidal source (switched on a long time ago), they recover the time harmonic solution with inverse square root behaviour in the far field.

In the absence of a suitable analytical method with which to compare their wholly-numerical solutions, two of the present authors sought help from their co-author, who, in due course, realised a possible approach (Rienstra [2]) that is summarised in the Appendix. It is applicable to a particular class of functions defining the time dependence of the mass flowrate from a line source. The principal advantage of this method over all previous ones is that the singular behaviour near the origin – a potential problem in case of the general solution in integral form – yields no numerical problems in the evaluation of the test solution. Furthermore, accuracy tests can go as high as the number of available digits, while any asymptotic behaviour can be recognised directly from the formulas, rather than by visual (inevitably less accurate) observation of graphical plots.

The method is used below to provide analytically exact solutions at finite radii that can be used as prescribed inner boundary conditions for numerical analyses. Comparisons of the analytical and numerical solutions at greater radii can then be used to assess the accuracy of the numerical methods. Herein, the velocity history at the inner boundary is prescribed and the assessments are based on velocity and pressure fields at greater radii. After validation, more complex inner boundary conditions are used in numerical solutions presented in Section 4.

1.3. Numerical methods

In principle, the particular problem that the engineering authors originally needed to study – *i.e.* wave emissions from railway tunnel portals – is amenable to investigation by any of a wide range of commercially-available CFD software packages. However, such software is highly demanding of computer resources and so is poorly suited to undertaking extensive parametric or sensitivity studies. This is true even when, as herein, the time scales of wave propagation are sufficiently small for the influence of viscous effects to be neglected for practical purposes. This avoids the need to choose between so-called RANS, LES and DNS packages that simulate turbulence in increasing detail – with correspondingly strong consequences for computer memory and simulation times. Notwithstanding such disadvantages, the authors did indeed use such CFD when they began their investigation and it is also used below (Section 4) to assess the use of the new 1D method in a simulation of cylindrical radiation from a duct exit.

The hunger for resources is not the only disadvantage of CFD packages. Another is that it is not usual for them to be optimised expressly for studying wave propagation. In previous work, the authors have found it difficult to totally suppress numerical oscillations in regions of very rapid pressure changes in steep-fronted waves propagating along a duct. The spatial grid sizes necessary to min-

imise these can be much smaller than those required in suitable 1D methods. Furthermore, for similar reasons, the optimal integration time intervals can be significantly smaller than those required by the CFL-stability criterion that applies in 1D methods. An even more important disadvantage of two- or three-dimensional CFD packages is that they cannot realistically be used in practical simulations of waves in extensive duct networks when the same simulation must also simulate radiation beyond the various duct exits. No such studies are needed herein, but they are commonly needed in practical applications. Instead, the goal herein is simply to identify strengths and weaknesses of the new 1D methodology when it is used for (a) purely cylindrical radiation and (b) coupled uniaxial and cylindrical radiation.

The numerical method developed in Section 2 utilises the Method of Characteristics (MoC). This generic tool has greatest potential in applications that can be simulated using only two independent variables, although, in principle, it can be used to simplify the representation of systems with more than two. In the literature, applications to time-dependent flows in one spatial coordinate are referred to as one-dimensional MoC. A large majority of practical applications of this method deal with uniaxial wave propagation in ducts and channels, although rare examples exist of its use for spherical propagation. The authors are not aware of any previous numerical applications to the more complex case of cylindrical radiation or to the coupling of the method to uniaxial MoC, as is done in Section 4.

Regardless of the particular numerical method, there are just two boundary conditions, namely at the minimum and maximum radii in the calculation domain. The inner boundary is relatively straightforward. It determines the nature of the disturbance propagating into the domain. It may be expressed in many ways, including for instance, (i) the time dependence of the pressure or flowrate and (ii) a constant or time-dependent relationship between these two. Regardless of this choice, the outward-propagating disturbance continually causes inward-propagating disturbances that interact with the outward ones. The outer boundary condition needs to be implemented in a manner that does not interfere with this process. In numerical simulations, it is convenient to do this by locating the boundary at a radius that exceeds the greatest distance that the disturbance will reach before the simulation is terminated.

2. Method of Characteristics (MoC)

In a previous study by Vardy & Tijsseling [9], a numerical implementation of the method of characteristics (MoC) was applied to waves propagating in a purely

spherical manner. At that time, it was not expected that an equivalent approach would be a good choice for cylindrical radiation even though, generically, both can be represented by MoC equations of the form (*e.g.* Owczarek [10], Whitham [7]).

$$\frac{\mathrm{d}p}{\mathrm{d}t} \pm \rho c \frac{\mathrm{d}u_r}{\mathrm{d}t} = f^{\pm}(r, u_r) \tag{1}$$

where p = pressure, ρ = density, c = speed of sound, u_r = radial velocity, r = radial coordinate, t = time coordinate and the function $f^{\pm}(r, u_r)$ includes all required source terms. These equations are valid in the characteristic directions

$$\frac{\mathrm{d}r^{\pm}}{\mathrm{d}t} = u_r \pm c \tag{2}$$

respectively, where the upper signs in Eq. (2) correspond to the upper signs in Eq. (1) (and similarly for the lower signs).

This formulation of the equations has been used in each of the few previous implementations of radial wave propagation known to the authors. Most deal with spherical radiation – *e.g.* Kluwick [11], Li et al. [12], Zhang et al. [13] – although cylindrical radiation has also been studied – *e.g.* Whitham [7], Steiner & Gretler [14] and Kraiko [15]. In all of these cases, attention was restricted to the case of purely radial propagation. This is also true in Section 3 herein, in which direct comparisons are made with analytical solutions. In Section 4, however, the radial flow analysis is coupled directly to a uniaxial flow analysis, thereby enabling the simulation of the reflection and transmission of internally-propagating waves reaching a duct exit to an external environment.

Unfortunately, the particular formulation expressed in Eqs. (1) & (2) is less than ideal for numerical simulations because the function f usually includes terms in r^{-1} and r^{-2} that are singular at $r = 0$. This is the case even when no distributed source terms exist in the fundamental equations from which the MoC equations are developed. In principle, such singularities can be accommodated in analytical formulations of the equations, but they have to be avoided in numerical formulations. This is done by excluding a zone of small radii from the numerical solution domain, thereby incurring an important penalty of needing to infer suitable boundary conditions at a finite inner radius. This matter is addressed further in Section 3. Furthermore, the smaller the radii at which numerical solutions are required, the smaller the grid sizes that must be used to achieve acceptable accuracy. The severity of the consequences of this depends upon the particular numerical formulations of the equations, and this is the motivation behind the following redevelopment of

the analytical equations into a form from which the numerical representations are subsequently developed.

2.1. Cylindrical MoC

The continuity and momentum equations for cylindrically symmetric flow can be expressed as

$$\frac{\partial}{\partial t}(r\rho) + \frac{\partial}{\partial r}(r\rho u_r) = C \tag{3}$$

and

$$r\frac{\partial}{\partial r}(p) + \frac{\partial}{\partial t}(r\rho u_r) + \frac{\partial}{\partial r}(r\rho u_r^2) = M \tag{4}$$

in which C & M denote source terms. For example, C can be used to describe continuous mass addition or removal and M can define body forces or forces associated with energy-dissipation mechanisms. It is informative to retain these generic terms in the following general development even though, for clarity, both are deemed to be zero in the particular numerical examples considered below.

Equations (3) & (4) relate derivatives of three independent variables, namely p, ρ and u_r. To proceed, it is necessary to introduce a third relationship which, in general, could be an energy equation enabling account to be taken of, say, heat addition/subtraction or of dissipative phenomena giving rise to the term M above. In many applications, however, it is acceptable to neglect possible causes of entropy change on wave propagation and, in the case of gases that may reasonably be regarded as perfect, the pressure and density can be assumed to satisfy the homentropic relationship $p/\rho^\gamma = \text{constant}$, where γ is the ratio of the principal heat capacities. Also, the speed of sound then satisfies $c^2 = \mathrm{d}p/\mathrm{d}\rho = \gamma p/\rho$ and the derivatives of ρ and p can be replaced by, for instance,

$$\frac{\partial p}{\partial t} = \frac{2}{\gamma - 1}\rho c\frac{\partial c}{\partial t} \tag{5}$$

and

$$\frac{\partial \rho}{\partial t} = \frac{2}{\gamma - 1}\frac{\rho}{c}\frac{\partial c}{\partial t} \tag{6}$$

With these substitutions, Eqs. (3) and (4) can be developed as

$$\frac{2}{\gamma - 1}\frac{\partial}{\partial t}(c) + \frac{2}{\gamma - 1}u_r\frac{\partial}{\partial r}(c) + \frac{c}{r}\frac{\partial}{\partial r}(ru_r) = \frac{c}{r\rho}C \tag{7}$$

and

$$\frac{2}{\gamma-1}c\frac{\partial}{\partial r}(c)+\frac{1}{r}\frac{\partial}{\partial t}(ru_r)+\frac{u_r}{r}\frac{\partial}{\partial r}(ru_r)=\frac{u_r^2}{r}+\frac{1}{r\rho}(M-u_rC) \tag{8}$$

which is a pair of equations relating derivatives of c and ru_r. In the method of characteristics approach, these hyperbolic equations are combined and re-expressed as ordinary differential equations, namely

$$\frac{2}{\gamma-1}\frac{\mathrm{d}}{\mathrm{d}t}(c)\pm\frac{1}{r}\frac{\mathrm{d}}{\mathrm{d}t}(ru_r)=\pm\frac{u_r^2}{r}+\frac{1}{r\rho}\Big[\pm M^{\pm}+(c\mp u_r)C^{\pm}\Big] \tag{9}$$

that are valid only in the directions of gradients of characteristic paths $r=r^{\pm}(t)$ given by

$$\frac{\mathrm{d}r^{\pm}}{\mathrm{d}t}=u_r\pm c \tag{10}$$

respectively. The uppermost signs in Eq. (9) correspond to the uppermost signs in Eq. (10) and likewise for the lowermost signs.

This derivation is straightforward, but attention is drawn to two aspects that have strong practical benefits, notably enabling the use of coarser numerical grids than those that are acceptable with the corresponding equations developed directly from Eqs. (1) and (2). First, although several terms involve r^{-1}, none involves r^{-2}. Second, since ru_r is proportional to the radial mass flowrate, the derivative $\mathrm{d}(ru_r)/\mathrm{d}t$ in Eq. (9) typically varies more slowly than $\mathrm{d}u_r/\mathrm{d}t$ in Eq. (1), especially at small radii. Indeed it tends to zero in periods of slowly varying flow whereas the velocity $\mathrm{d}u_r/\mathrm{d}t$ is non-zero even in exactly steady flows. The relative importance of this depends on the ratio $(\Delta r)/r$, where Δr denotes the change in radius over a single grid length. This ratio increases rapidly as $r\to 0$ and this is a strong determinant of the grid size necessary (over the whole calculation domain) to achieve acceptable numerical accuracy.

It is worth noting in passing that the first term (u_r^2/r) on the right-hand side of Eq. (9) is not a consequence of source terms in the original continuity and momentum equations (3) and (4). On the contrary, it exists even when no such source terms need to be considered. This is an important difference from the corresponding spherical formulation of the equations given by Vardy & Tijsselling [9]. It is a mathematical indicator of the dispersive-like behaviour mentioned in the introduction and illustrated in the examples presented in Section 3. However, although it is not a formal source term in the analytical development, it is grouped with source terms in the following numerical integration process.

The use of the product ru_r as a primary integration variable in preference to u_r alone is also important when it is necessary to use interpolation to infer values between adjacent grid points in numerical grids. This is highlighted in the following section after describing the meanings of the points L and R in Fig. 2.

2.2. Numerical integration

In practice, equations (9) & (10) are integrated numerically in a time-marching manner, proceeding one step at a time. Herein, a fixed rectangular grid shown as broken lines in Fig. 2 is assumed, although that is only one of several reasonable options. Others include, for instance, a diamond grid or a so-called natural grid that tracks individual wave paths. The latter has the advantage of avoiding the need for interpolations that are necessary when using regular grids, but its solutions are obtained at irregularly distributed points in (r, t) space.

In principle, the numerical solution at a typical point 'A' at the time t_2 in Fig. 2 depends only on values at grid points at the earlier time t_1. Characteristic lines that nominally satisfy Eqs. (10) are projected backwards in time to the points L and R at $t = t_1$. The projections cannot be undertaken exactly because the variations of u_r and c along LA and RA are unknowable in the numerical representation. Instead, the average gradients of the lines are estimated from values of u_r and c at L and A. Even these values are unknown when the gradients are first estimated, so the first iteration in the solution for values at A is only approximate. Nevertheless, after estimating the locations of L and R and inferring values of flow parameters at these locations, Eqs. (9) (expressed along LA and RA) can be integrated and solved simultaneously to give a first estimate of the corresponding values at A. Successive repeats of the process are undertaken until the solution converges and the whole sequence is then repeated for all remaining grid points at t_2.

Although straightforward in principle, the steps followed in this sequence require decisions that merit attention. One relates to the determination of parameter values at the points L and R. Herein, for simplicity, this is done by interpolating linearly between adjacent grid points. Clearly, this is only approximate, but it is not possible to know 'correct' distributions at the time of writing the software. The true shapes of the distributions depend upon local variations in space and time and these, in turn, depend on user-prescribed boundary conditions that will commonly be time-dependent. For the purpose of locating L and R – *i.e.* integrating Eq. (10) backwards in time – the parameters to be interpolated are u_r and c. Their values are also required for the integration of Eq. (9), but the principal interpolations for this are c and the product ru_r. This product is of key importance so direct interpolation for it is preferable to evaluating the product of r and

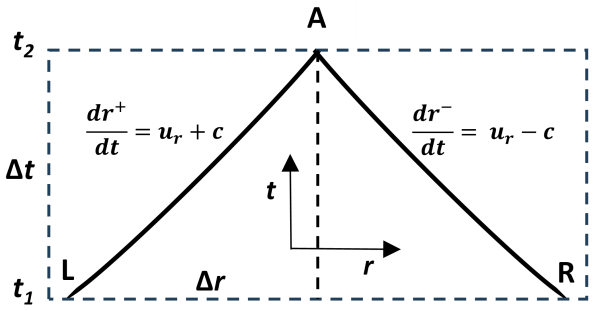

Figure 2: Numerical grid and characteristic wave paths in (r, t) space
$(\Delta t/\Delta x)$ *increased to exaggerate the need for interpolation at L and R)*

u_r obtained independently.

A second decision required in the numerical process is how to approximate the integrals of $\frac{1}{r}\frac{\mathrm{d}}{\mathrm{d}t}(ru_r)$ along LA and RA. Once again, this can be done in any of several ways. However, all reasonable choices will lead to the same converged result if (i) sufficient iterations are undertaken and (ii) the grid-size assessment is undertaken reliably. The optimum choice will depend upon the balance that the software writer wishes to achieve between CPU-efficiency and the human effort required (i) to achieve the CPU-efficiency, (ii) to check the code, and (iii) to extend or revise the code at a later date. If the software is intended for wider use, robustness will be a key requirement and this is likely to favour simplicity over maximising CPU efficiency, especially as numerical simulations such as those discussed herein are unlikely to take more than a few minutes – and possibly only a few seconds. Herein, a first-order scheme is chosen to take advantage of the simplicity that this affords. To allow for the various numerical approximations, accuracy is assessed by undertaking repeat simulations with successively smaller grid sizes until solutions differ by acceptably small amounts.

Summarising, the chosen numerical representations of Eqs. (9) and (10) are:

$$\frac{2}{\gamma-1}(c_A - c_L) + \left(\frac{1}{r}\right)_{LA}(r_A u_{rA} - r_L u_{rL}) \approx$$
$$+ \left(\frac{u_r^2}{r}\right)_{LA}(t_A - t_L) + \left\{\frac{1}{r\rho}\left[+M + (c - u_r)C\right]\right\}_{LA}(t_A - t_L) \quad (11)$$

and

$$\frac{r_A - r_L}{t_A - t_L} \approx \frac{1}{2}\left[(u_{rA} + c_A) + (u_{rL} + c_L)\right] \quad (12)$$

in which the suffix LA denotes an average value over the integration interval.

In contrast with the corresponding equation for uniaxial 1D propagation, the right hand side of Eq. (11) is never zero (except in the trivial case of zero flow). Nevertheless, good accuracy is achievable in principle provided that the chosen time steps of integration are sufficiently small. In practice, this is a more demanding requirement at small radii than at larger ones and it becomes unachievable as $r \to 0$. However, it is eminently achievable in many practical cases, as evidenced by comparisons presented in the following Sections.

When, as usual, γ is treated as constant, the first term on the left hand side of Eq. (11) is algebraically exact. However, the second term is not because $(1/r)_{LA}$ is treated numerically as a constant even though $1/r$ necessarily varies along LA. This illustrates why it is important to undertake independent solutions of the overall phenomenon with successively smaller grid sizes. It is also necessary to choose a suitable method of evaluating $(1/r)_{LA}$. Obvious possible choices include (i) $2/(r_L + r_A)$ or (ii) $\frac{1}{2}(1/r_L + 1/r_A)$, but these are not used in the software used herein. Instead, it is evaluated as $\ln(r_A/r_L)/(r_A - r_L)$, implying that the characteristic is a straight line between L and A. None of these expressions is exact, but all should tend to the same solution as the grid size is reduced.

The right-hand side term $(u_r^2/r)_{LA}$ cannot be handled in a similar manner. Instead, it is evaluated as a simple average $\frac{1}{2}[(u_r^2/r)_L + (u_r^2/r)_A]$. The influence of this term depends on its relative magnitude in comparison with the left hand side terms. It is especially significant during periods of relative calm after a primary disturbance has passed – *i.e.* during the decay towards the original ambient conditions. In such periods, it can play a dominant role, but then the velocity is varying only slowly so a simple average of its values at L & A can be a close approximation to the true value.

Up to this point, no limitations have been imposed on the allowable forms or magnitudes of the source terms C & M. In practice, however, both will commonly be either zero or sufficiently small for their influence to be negligible. Therefore, to avoid unnecessary complications, they are discounted in the remainder of this development even though their retention in generic form would be straightforward. Readers who so wish could easily include these terms to explore their influence, especially in context-specific cases where they can be expressed in algebraic form.

With this simplification, Eq. (11) and its counterpart along RA can be written

as

$$\frac{2}{\gamma-1}(c_A)+\left(\frac{1}{r}\right)_{LA}(r_A u_{rA})-\frac{u_{rA}^2}{2r_A}(\Delta t)_{LA}\approx \frac{2}{\gamma-1}(c_L)+\left(\frac{1}{r}\right)_{LA}(r_L u_{rL})+\frac{u_{rL}^2}{2r_L}(\Delta t)_{LA} \quad (13)$$

and

$$\frac{2}{\gamma-1}(c_A)-\left(\frac{1}{r}\right)_{RA}(r_A u_{rA})+\frac{u_{rA}^2}{2r_A}(\Delta t)_{RA}\approx \frac{2}{\gamma-1}(c_R)-\left(\frac{1}{r}\right)_{RA}(r_R u_{rR})-\frac{u_{rR}^2}{2r_R}(\Delta t)_{RA} \quad (14)$$

On subtraction to eliminate c_A, these equations yield a simple quadratic equation that can be solved for the velocity u_{rA}. The sound speed c_A is then obtained by back-substitution and the density and pressure follow from property relationships. This solution method is implemented at all required locations – *e.g.* at successive locations in the fixed grid in (r, t) space. As emphasised above, the whole solution process is then repeated with successively smaller grid sizes until further reductions cause acceptably small differences.

For completeness, it is pointed out that the above derivations do not explicitly limit the allowable Mach number or pressure, although it *is* assumed that the flow is continuous (*e.g.* no shocks). The grid-size required to meet any particular numerical accuracy criterion will reduce with increasing Mach number, but this is solely a numerical requirement, not a limitation on the physical values of the flow parameters. However, the analytical solution used below for formal validation purposes is based on acoustic approximations and even the subsequent comparison with a more general 2D case is for a small Mach number.

2.3. Boundary conditions and initial conditions

In any particular simulation, the analyst is responsible for specifying initial conditions everywhere as well as boundary conditions at the inner and outer radii of the calculation domain. Commonly, as in all cases herein, the initial conditions will simply be a stationary ambient state. Also commonly, the boundary conditions will be designed to be suitable for simulating the progress of a disturbance propagating outwards from the inner boundary. In such cases, the inner boundary condition may be, for example, (i) a prescribed flowrate history, (ii) a prescribed

pressure history or (iii) a prescribed relationship between pressure and flowrate. The first of these is used in Section 3 for particular cases for which analytical solutions are available. That is, at any instant, the velocity u_{rA} is known a priori at the boundary and the sound speed follows from whichever of Eqs. (13) and (14) is appropriate. The pressure follows from property relationships. The second type of boundary condition – i.e. prescribed values of p_A – is similar except that c_A is deduced from p_A before use is made of the appropriate characteristic equation. An example of the third type of boundary condition is presented in Section 4.

In almost all practical simulations, an ideal outer boundary condition will be such that (a) it is transparent to outward-moving waves and (b) it does not induce any changes in pressure or velocity other than those that result from the outward-propagating disturbance. The second of these criteria is highlighted because any independent, inward-moving waves would interact with the phenomenon under study. Herein, the criteria are satisfied exactly by locating the outer boundary at a radius that exceeds the maximum distance travelled by the leading tip of a disturbance during the period simulated, namely $c_0 t_{\max}$. In this case, ambient conditions prevail at the boundary throughout the simulation. The authors are not aware of any other method of meeting the above-stated criteria exactly, so, in practice, the chosen method is the sole determinant of the minimum required size of the simulation domain.

3. Radiation from a cylinder: Sources with *N*-shaped (*N*) and bulge-shaped (*B*) time-profiles

The analytical solutions developed recently by Rienstra [2] and summarised in the Appendix are now used to assess the accuracy of the MoC analysis in the linear regime. The analytical method enables solutions to be obtained for a class of line sources defined by a prescribed variation in time of the rate of change of mass flowrate at the origin $r = 0$. The analysis yields pressures and velocities at all $r \geqslant 0$ and it is found that the shapes of the pulses vary as they propagate. For validation purposes, velocity histories at a finite radius $r = a$ obtained from the analytical solution are used as prescribed inner boundary conditions in the MoC analysis. Numerical solutions in the zone $r \geqslant a$ are then compared with the (exact) analytical solution. This may be loosely interpreted as the zone outside a radially vibrating cylinder of radius a. In the following numerical examples, $a = 1\,\mathrm{m}$ and the gas is modelled as air with an ambient density and speed of sound of $\rho_0 = 1.2\,\mathrm{kg/m^3}$ and $c_0 = 340\,\mathrm{m/s}$ respectively. The leading tip of the disturbance arrives at $r = a$ at the instant $t = a/c_0 \approx 2.94\,\mathrm{ms}$.

The first two examples apply to pulses from sources that, at the origin, are N-shaped in time – see Fig. 3a. This is a family of curves that derives its name from the particular case of $n = 1$. Although, for simplicity, these are referred to herein as 'N-shaped sources', it is emphasised that (i) the name identifies their time history, not the resulting spatial profile (which evolves anyway) and (ii) only the simplest member of the family is a close approximation to the shape of the character N.

As shown in the Appendix, the pulses result from a mass source of finite duration b at the origin ($r = 0$) defined by the "N-shaped sources" (see Eq. (A.11))

$$\begin{aligned}
\frac{\partial \dot{m}}{\partial t}\Big|_{r=0,t\leqslant b} &= \rho_0 c_0^2 A\sqrt{2n-1}\Big(\frac{4n-2}{n-1}\Big)^{n-1}\Big(1-2\frac{t}{b}\Big)\Big(\frac{t}{b}\Big)^{n-1}\Big(1-\frac{t}{b}\Big)^{n-1}, \\
\frac{\partial \dot{m}}{\partial t}\Big|_{r=0,t>b} &= 0.
\end{aligned} \tag{15}$$

For $n = 1$ the right-hand side of Eq. (15) reduces to $\rho_0 c_0^2 A(1 - 2t/b)$. Within $0 < t < b$, each N-shaped source except the limiting case of $n = 1$ rises smoothly from zero to a maximum, then reduces beyond zero to a minimum and finally rises again to zero. The parameter A is an arbitrary scaling factor, small enough to warrant the linearisation, and the power n modulates the basic shape corresponding to $t(b-t)$. In particular, it controls the smoothness at the switch-on/switch-off points $t = 0$ and $t = b$. In the following simulations based on N-shaped sources, $n = 2$. This formulation is one of a class for which Rienstra [2] has obtained analytical

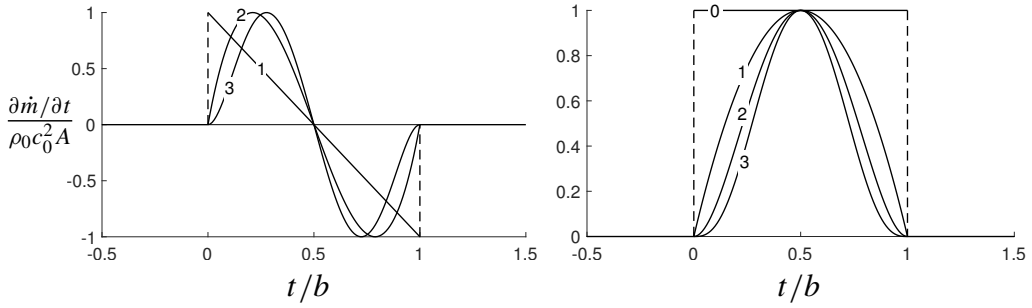

(a) N-shaped profiles, $n = 1, 2, 3$ (b) B-shaped profiles, $n = 0, 1, 2, 3$

Figure 3: Families of N-shaped and B-shaped source profiles: rates of change of mass flowrate per unit source length ar $r = 0$. N_1 and B_0 are discontinuous at $t = 0$ and $t = b$.

solutions. His derivations are developed in a non-dimensional form in which time is normalised by the pulse duration. That is, the non-dimensional time is defined

as $t' = t/b$. This is both convenient and instructive in the context of the analytical derivation. However, some aspects of behaviour in the examples discussed below are discussed more easily in dimensional time than in non-dimensional time because the existence of the inner boundary condition in the numerical method has the effect of creating a second time scale.

3.1. Short-duration pulse

The upper row of graphs in Fig. 4 shows histories of the pressure, velocity and acceleration at $r/a = 1$, 3 and 5 for the particular case of $n = 3$ and $b = 1$ ms, which is approximately 30 % of the time required for a sound wave to travel a distance equal to the cylinder radius $a = 1$ m. The lower row shows the same data, but scaled to highlight common behaviour at the various locations. The pressure, etc. axes are scaled by the square root of the local radius and the time axes are retarded times. That is, the time axis of each graph is offset by r/c_0, namely the time required for sound waves to travel the radial distance from the origin. With these adjustments, the various curves are so similar that it is difficult to distinguish between them even when they are plotted at a much larger scale than is feasible in the printed figure. This outcome is typical of solutions at large non-dimensional times for relatively high frequency, N-shaped sources (for which the time average of the mass flowrate is zero).

The results presented in the figure were obtained using a grid size such that the duration b of the initial-pulse corresponded to approximately 34 time steps and the simulation then required about 12 seconds on an ordinary laptop computer. The graphs are visually indistinguishable from those when the grid size was doubled. However, a further doubling of the chosen grid size caused small phase shifts that were detectable at the increased scales used in the graphs presented for retarded times.

If these were the only data available, it would be tempting to conclude provisionally that the pulse is travelling in unchanged form except for reducing in amplitude with the square root of the radius. That would be analogous to the true behaviour of purely spherical radiation of small-amplitude pulses in which the amplitudes vary with the reciprocal of the radius itself. However, as indicated above, the true cylindrical radiation is more complex than this interpretation would imply. More detailed discussion of the behaviour is deferred until after presenting the corresponding solution for a longer duration pulse (in Section 3.2), thereby enabling attention to focus on comparisons of two cases.

All boxes in Fig. 4 show three curves obtained from the numerical solution. This enables deductions to be drawn about the physical behaviour, but it would

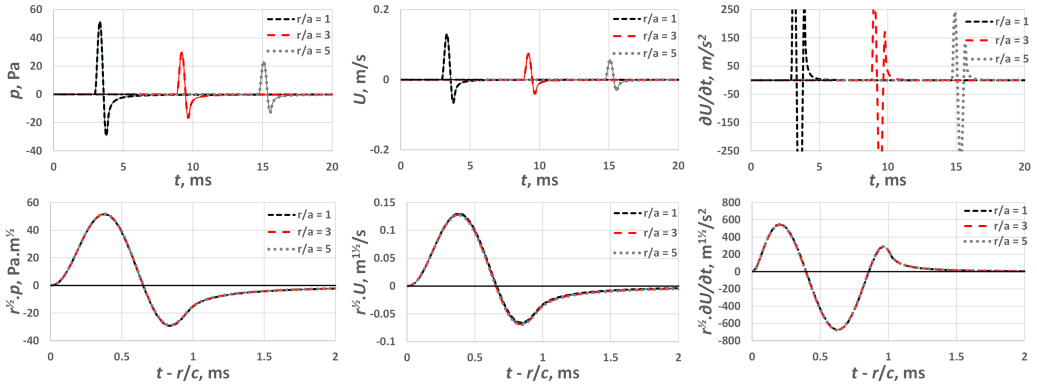

Figure 4: Radiated pressure, velocity & acceleration from a cylinder of radius 1 m (N-shaped source, $n = 3$, $b = 1$ ms)
(NB: (1) The analytical velocity history at $r = a$ is used as a prescribed boundary condition in the MoC analysis; (2) In both rows, the graphs of pressure and velocity include both analytical and numerical solutions, although the curves are almost indistinguishable)

not, by itself, give any information about the accuracy of the solution. For that, comparisons are made with analytical solutions of the pressure and velocity obtained using the method outlined in the Appendix. These are shown as continuous lines in the left-hand and middle boxes of the figure together with the numerical solutions (broken lines). That is, each of these boxes includes a total of six curves. By inspection, differences between the numerical and analytical curves are so small that it is reasonable to conclude that the numerical method and its implementation herein are sufficiently accurate for practical purposes. In practice, since the analytical solution is itself new, the agreement could also be interpreted as supportive of its validity. For completeness, it is reiterated that the analytical solution is based on acoustic approximations so this example and those presented in Figures 5 & 6 do not constitute validation of the finite-amplitude capabilities of the MoC analysis.

3.2. Longer-duration pulse

Figure 5 shows corresponding comparisons for a pulse that is identical to that simulated above except that its duration is ten times longer (*i.e.* $b = 10$ ms). This corresponds approximately to the time required for a sound wave to travel a distance equal to three cylinder radii. For consistency, the numerical grid is unchanged even though the reduced rates of change of flow parameters could justify using an increased grid size. In common with Fig. 4, all boxes in the figure show numerical solutions at three locations and the pressure and velocity boxes in each

row also show analytical solutions. Readers viewing the paper in digital form may be able to enlarge the figure and hence verify that the differences between the numerical and analytical solutions are tiny.

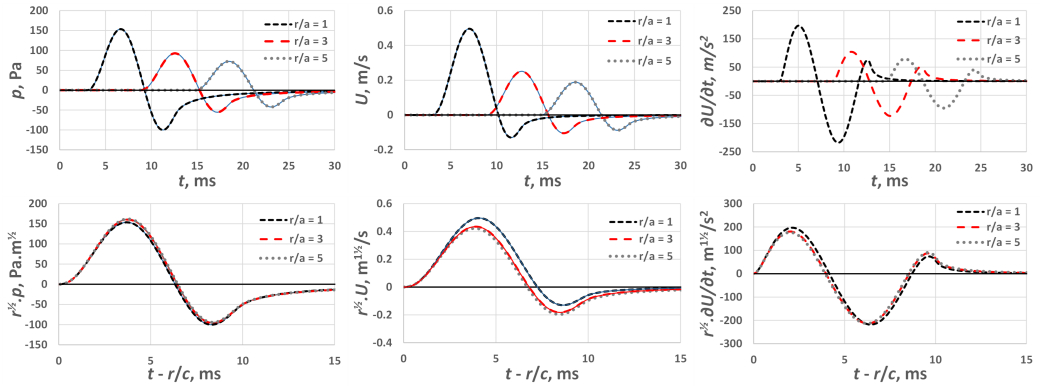

Figure 5: Radiated pressure, velocity & acceleration from a cylinder of radius 1 m (N-shaped source, $n = 3$, $b = 10$ ms)
(NB: (1) The analytical solution for the velocity history at $r = a$ is used as a prescribed boundary condition in the MoC analysis; (2) In both rows, the graphs of pressure and velocity include both analytical and numerical solutions, although the curves are almost indistinguishable)

The overall behaviour is broadly similar to that given in Fig. 4 for the shorter-duration pulse, but an important effect that is almost hidden in Fig. 4 is exhibited clearly in Fig. 5. This relates to asymptotic conditions at large times as the pulses propagate outwards. Focussing firstly on the scaled velocity in the lower middle box of Fig. 5, it is seen that the graphs for $r/a = 3$ and $r/a = 5$ are almost similar, but that they differ significantly from the graph at $r/a = 1$. This illustrates progress towards an asymptotic state described by Whitham [7] and Lighthill [8] and stumbled upon by Wang et al. [16] when attempting to explain behaviour that, for them, was unexpected. In fact, references to it in the literature appear to be very sparse. Rienstra [2] has provided quantitative analyses for sources of the types presented here. He showed that, after scaling by the factor $r^{0.5}$, the pressure and velocity converge to exactly the same function of $(t - r/c_0)/b$ at sufficiently large values of t/b (except for a multiplication factor).

The graphs presented In Figs. 4 & 5 are for the same three values of the ratio r/a, namely 1, 3 & 5. However, the corresponding values of $r/(c_0 b)$ are ten times greater in Fig. 4 than in Fig. 5. As a consequence, from a non-dimensional point of view, the solutions presented in Fig. 4 are much closer to the asymptotic condition. This is why its scaled graphs at the various locations are so similar to one another even though the same does not apply in Fig. 5.

Rienstra [2] also showed that the non-dimensional velocity approaches its asymptotic state more slowly than the non-dimensional pressure. Again, this behaviour is not easily inferred from Fig. 4 even though two consequences of it are displayed clearly in Fig. 5. First, the scaled graph of velocity for $r/a = 1$ differs clearly from the graphs for $r/a = 3$ and $r/a = 5$ whereas the corresponding differences for the pressure are only just identifiable (unless the numerical data are inspected). Second, the shapes of the pressure and velocity graphs are more similar at $r/a = 5$ than at $r/a = 1$.

For future reference, it should be noted that, in all of the time-shifted graphs in Figs. 4 and 5, the early parts of the pulse – until about half the maximum amplitude – at all three radii are closely similar. Thereafter, however, differences between the histories are more obvious and they increase as the pulse propagates. The break point between these two types of behaviour is more pronounced than would pertain if the differences developed at a uniform rate throughout the pulse. The discussion of a further example presented in Section 3.4 sheds light on this behaviour.

In both of Figs. 4 and 5, it is seen that, visually, a family resemblance exists between the pressure and velocity histories, but that little correlation exists between the pressure and acceleration histories. A similar outcome was found by Vardy & Tijsseling [9] for the simpler case of spherical radiation of half-sine-wave pulses with durations of 1 ms and 10 ms at distances of $r = 1$ m, 3 m & 5 m from the surface of a sphere of radius $a = 1$ m. In both cases, the analytical solutions show that this correlation becomes increasing close as time increases. Attention is drawn to the behaviour at this stage as a background for interpreting solutions for a more complex case in Section 4 below, in which the radial MoC analysis (r, t) is coupled with a uniaxial MoC analysis (x, t).

3.3. Source with a B-shaped profile

Figure 6 shows corresponding solutions for a particular case of a pulse-like source that is one of a second family classified in the Appendix. Herein, these are designated as 'B-shaped' (short for 'Bulge-shaped'); see Eq. (A.10). For these sources, which are illustrated in Fig. 3b, the rate of change of mass flowrate at the origin ($r = 0$) satisfies

$$\begin{aligned} \frac{\partial \dot{m}}{\partial t}\Big|_{r=0,t\leqslant b} &= \rho_0 c_0^2 A 4^n \Big(\frac{t}{b}\Big)^n \Big(1 - \frac{t}{b}\Big)^n, \\ \frac{\partial \dot{m}}{\partial t}\Big|_{r=0,t>b} &= 0. \end{aligned} \tag{16}$$

Once again, n controls the smoothness at the instants $t = 0$ and $t = b$. For $n = 0$, the rate of change of the mass flowrate – $\partial\dot{m}/\partial t$ – is effectively shaped like a block, discontinuous at $t = 0$ and $t = b$. For $n > 0$, it rises continuously from zero at $t = 0$ to a maximum at $t = b/2$ and then reduces to zero at $t = b$. It is zero for all $t < 0$ and all $t > b$. For completeness, it is noted that, apart from a normalisation, the above N-shaped-sources Eq. (15) are time derivatives of B-shaped-sources Eq. (16).

For the particular case used in Fig. 6, $n = 0$ so, within the interval $0 < t < b$, the prescribed rate of change of mass flowrate is constant and equal to $\rho_0 c_0^2 A$. The duration of the pulse is $b = 10\,\text{ms}$, which is the same as the duration of the N-shaped source considered in Fig. 5. Once again, each box shows numerical solutions at three radii and the four boxes showing pressure and velocity also include the corresponding analytical solutions. It can be seen that there is negligible difference between the numerical and analytical solutions so attention again focuses on the physical behaviour.

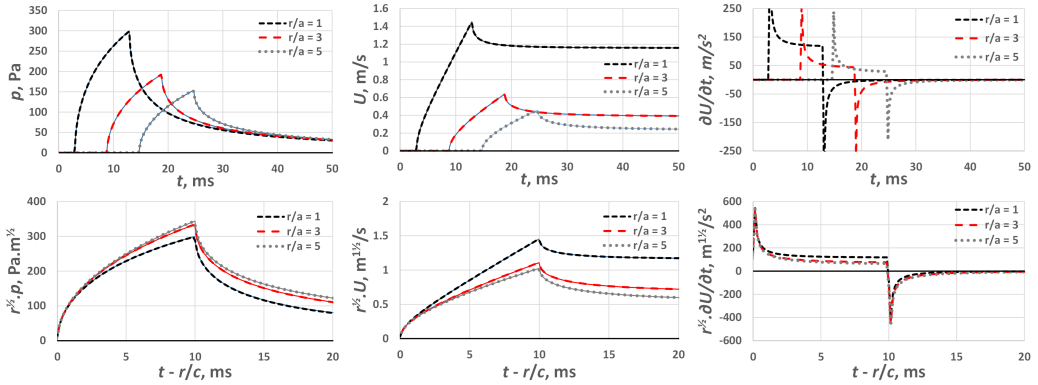

Figure 6: Radiated pressure, velocity & acceleration from a cylinder of radius 1 m (B-shaped source, $n = 0$, $b = 10\,\text{ms}$)
(NB: (1) The analytical velocity history at $r = a$ is used as a prescribed boundary condition in the MoC analysis; (2) In both rows, the graphs of pressure and velocity include both analytical and numerical solutions, although the curves are almost indistinguishable)

By inspection, the pressures and velocities at $r/a = 1$, 3 & 5 differ from asymptotic states more than those in either of Figs. 4 & 5. That is, they are approaching their asymptotic states more slowly. Nevertheless, the evolution towards asymptotic behaviour is again apparent because the values at $r/a = 3$ & 5 are closer together than those at $r/a = 1$ & 3. Furthermore, a comparison of the scaled graphs of pressure and velocity again shows the pressure converging more rapidly than the velocity.

Figure 6 also illustrates a difference between the evolutions of pressure and velocity during the period before asymptotic conditions are approached closely. It is seen that the scaled pressures approach the asymptote from below whereas the scaled velocities approach it from above. This behaviour also exists in the above examples for N-shaped sources, but it is too small to be seen in Fig. 4 and, even in Fig. 5, it is clear only in the graphs for velocity.

It is informative to compare the behaviour of the above cylindrical radiation with the well-known behaviour of spherical radiation. In the case of spherical radiation from a point source, there exists a region close to the origin in which the flow field has a significant dependence on dynamics not strongly related to wave propagation. The extent of this region reduces with increasing frequency of the disturbances and also with increasing radius. At sufficiently large radii, wave behaviour is wholly dominant. The inner and outer regions are termed the near-field and far-field respectively. Figures 4 and 5 exhibit a similar behaviour insofar as differences between the curves for $r/a = 3$ and $r/a = 5$ are much smaller than those for $r/a = 1$ and $r/a = 3$. This implies that far-field approximations might be assumed with reasonable accuracy at radii exceeding, say, $5a$. However, the sustained difference in Fig. 6 between the outcomes at $r/a = 3$ and $r/a = 5$ indicates that the transition to far-field conditions extends to much larger radii – as is consistent with the relatively low frequencies in the source-pulse.

3.4. Convolution-like behaviour

The strong difference between the qualitative outcomes for short-duration and longer-duration sources illustrates the significance of the tails behind cylindrically-radiating waves. Before discussing this directly, it is useful to conduct a simple thought experiment. Imagine a line source composed of a continuous series of short-lived, B-shaped profiles, not necessarily of equal magnitude or duration, but separated by discrete intervals. If the intervals are sufficiently large, the tails of the various pulses will decay to almost nothing before the next pulse arrives, so each pulse will travel in a manner that closely resembles that shown in Fig. 4 above. However, if the interval is too short for the decay period to be substantially complete, the succeeding pulse will propagate into an already-disturbed field. In that case, the flow conditions will differ from those shown in Fig. 4.

In practice, *all* sources considered herein are of finite duration so even the short ones in Fig. 4 are influenced by this effect. That is, later parts of any particular pulse are travelling into a field that has already been disturbed by earlier parts of the pulse. As a consequence, the result at any particular radius and instant will depend upon the particular shape of all earlier parts of the pulse. Consider, for

instance, the pulse sources shown schematically in Fig. 7 as a series of blocks of constant pressure. When block E of pulse 1 reaches a particular radius, the local conditions will be influenced by the tail effects of blocks A, B, C & D and so the cumulative result will depend upon (i) the amplitude and (ii) the elapsed time corresponding to each of these. For instance, the contribution of block A will be smaller in pulse 1 than pulse 2 because its amplitude is smaller – and the reverse will apply for block D. Furthermore, the contributions of each of A, B, C & D will be smaller in pulse 3 than in pulse 2 even though the individual blocks are identical. Mathematically, the behaviour resembles a convolution of amplitudes and elapsed times. Lamb [3], Whitham [7] and Lighthill [8] express this in an elegant manner based on a geometrical interpretation of a line source as a line of point sources along its axis (*i.e.* the z-axis).

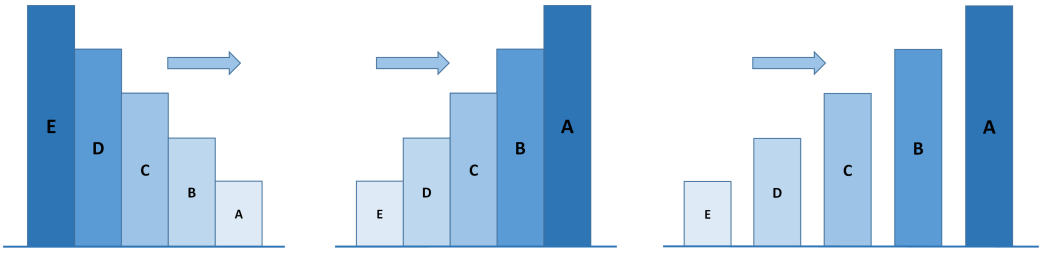

Figure 7: Schematic of alternative pulse sources

In the discussion of Fig. 5, it was noted that the deviation from a common curve was small until the steepest part of the rise and that it increased thereafter. This is consistent with the above interpretation. So is the behaviour seen in Fig.6, in which the steepest parts of the rise and fall occur at their leading edges. In contrast, the effect is completely absent in pulses radiating in a purely spherical manner. For them, the amplitude at any particular (r, t) depends solely on the amplitude of $\partial \dot{m}/\partial t$ at the source at the appropriate retarded time.

4. Radiation from a duct exit

All of the above simulations are applicable for a special class of cases for which the new analytical solutions exist. This has been used to prescribe the cylinder surface boundary condition for the MoC analyses and the velocity history has been used for this purpose. It would be equally valid to use the pressure history, but that would be less convenient numerically because it would necessitate additional iterations. In general, the boundary condition can also be expressed as

a relationship between pressure and velocity instead of prescribing one or other of them explicitly. This, too, requires an iterative approach, but the remainder of the paper nevertheless uses this capability to simulate a more complex case than the purely cylindrical example considered above.

After a compressive wavefront propagating along a duct with a flanged exit reaches the exit plane, it causes an increase in pressure and an acceleration of flow through the exit. However, the external environment limits and then reverses the pressure increase and the acceleration, both of which decay asymptotically to zero. This causes a delay in the reflection process and simultaneously causes the radiation of a pulse into the external environment. During the whole of the process, the acceleration is outwards so the outward velocity increases continuously and persists after the reflection. This general behaviour is well known, but almost all published literature relates to cases where the emitted pulse expands in three directions (*e.g.* from a gun or a musical instrument), not in only the two-dimensions available for the radiation studied herein. Wang et al. [16] hypothesised that radiation from a railway tunnel opening into a narrow cutting would approximate to cylindrical even though the wave propagation at larger distances would be more spherical-like.

In many practical applications, it is deemed sufficient to assume plane-wave behaviour for all wave propagation *inside* a duct. If it is also assumed that wave reflections at duct exits occur instantaneously, the simulated reflections will arrive at any location slightly earlier than the true timing observed in experiments. For a flanged duct of circular cross-section opening to an unbounded, 3D external domain, the delay experienced by low frequency, harmonic waves is approximately $0.85d/c_0$, where d is the duct diameter. This is the time that would be required for a sound wave to travel a distance of $0.425d$ back and forth and so the delay is commonly treated as if the duct were extended by this amount (the end correction). Regardless of the method used to describe the effect, the delay is a consequence of the incompatibility of purely uniaxial and purely radial propagation. Furthermore, just as waves arriving from along the duct experience effective delays when they 'reflect' at the exit plane, so too do waves from the external domain when they reflect at that interface. That is, when interpreted relative to external radial coordinates, the reflections appear to originate from a location inside the duct. Any apparent contradiction implied by the simultaneous existence of these 'opposite' delays is easily eliminated by interpreting the behaviour in terms of the (common) mass flowrate history at the exit plane instead of in terms of reflections remote from that plane.

In the following MoC analyses, wave propagation along the duct is modelled

in a conventional uniaxial manner, assuming plane wave behaviour, and the external field is modelled as purely cylindrical radiation. These representations are excellent at sufficiently large distances from the interface between the two zones - but they are only approximations in the transition zone between them.

Since the wave propagation in both regions is simulated one-dimensionally, conditions at the interface between them are, in effect, treated as changing abruptly between uniaxial and radial. At the interface, each zone provides one MoC compatibility equation, and the pair is solved in conjunction with additional boundary conditions that ensure continuity of pressure and flowrate. Continuity of flow area is also prescribed, but the interface is regarded as planar in the uniaxial zone and yet curved in the radial zone. That is, the directions of the velocity vectors change discontinuously even though their magnitudes are continuous. Two examples are depicted schematically in Fig. 8 and, in both cases, the internal and external domains are shown separately. One case corresponds to a duct with a simple flange and, for this, the inner boundary of the external domain is a full semi-circle so its included angle is $\varphi = \pi$. The other has a tapered external geometry for which $\varphi < \pi$. The internal and external domains are shown separately because their locations relative to each other are not determined explicitly in the 1D mathematical representation. The suitability of this composite 1D MoC methodology is assessed in detail in Section 4.2 by comparing solutions with corresponding ones obtained from a commercial CFD package – ANSYS Fluent v15.0 (ANSYS [17]) – that simulates the true 3D geometry. First, however, the use of the coupled MoC analysis is illustrated in its own right.

4.1. Coupled solution – MoC only

Figures 9a & 9b show simulated pressures and velocities at a distance of $3H$ upstream of the (flanged) exit plane of a rectangular-section duct of height $H = \pi$ m, giving a flow area of π per unit width (normal to the page in Fig. 8). With this height, the radius of the inner boundary of the external cylindrical radiation is equal to 1 m, thereby simplifying comparisons with numerical values used above. At approximately 0.07 s, a very steep fronted wave approaching the flanged exit of the duct causes an almost instantaneous pressure increase of 0.4 kPa and a simultaneous velocity increase of 1 m/s. The time $t = 0$ s corresponds to the instant when the wavefront is initiated at the upstream boundary in the numerical simulation, approximately $11H$ upstream of the exit. The subsequent reflection of the wavefront at the duct exit begins to arrive at approximately 0.13 s. Thereafter, three curves are shown. The simplest is an abrupt reduction in pressure back to the original value, accompanied by an increase in velocity from 1 m/s to 2 m/s

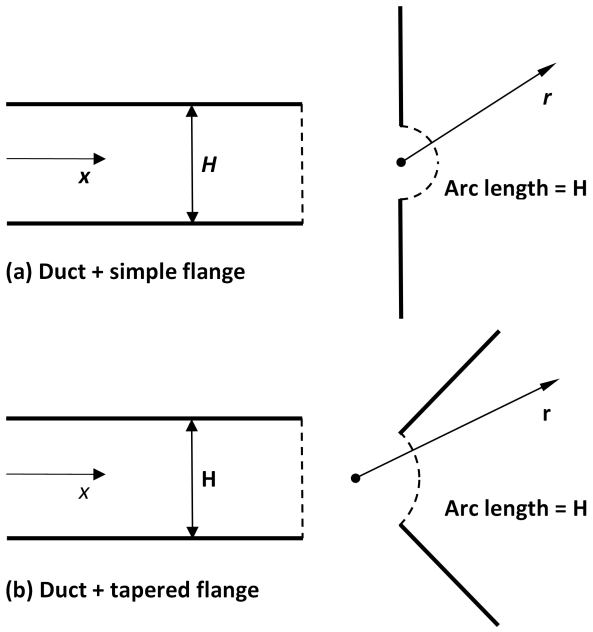

Figure 8: Radiation from a duct

(N.B. both the incident wavefront and its reflection cause increases in velocity). This particular curve does not occur physically; it is a convenient reference case that would occur if the whole reflection at the exit plane occurred instantaneously without causing any change in pressure at the interface.

The histories depicted by the broken lines are more closely indicative of true behaviour. The reflection begins to arrive at the expected time, but it approaches the 'final' state only asymptotically. This is a consequence of the delayed-reflection process discussed above. However, the asymptotic nature of the reflected wavefront contrasts sharply with the simple delays represented by end-corrections. The latter are good approximations for harmonic waves of sufficiently low frequency, whereas the almost step-like change considered here comprises a wide range of frequencies, including very high ones. Indeed, the whole of the initial step increase occurs in a distance that is far shorter than the duct height (N.B. compare the duration of the step increase with the interval between the incident wavefront and the start of the reflection. This corresponds to the time required for a wave to travel a distance of $6H$).

The intermediate curves in Fig. 9 are provided for reference only. They show the corresponding coupled 1D behaviour for a flanged duct of circular cross-

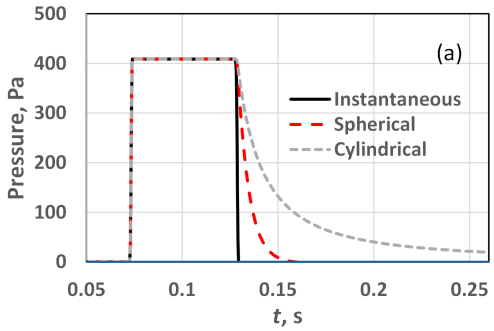

(a) Pressure $3H$ upstream of exit

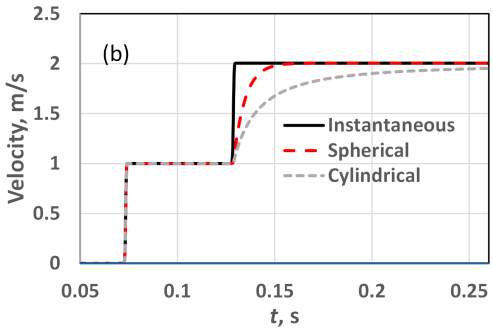

(b) Velocity $3H$ upstream of exit

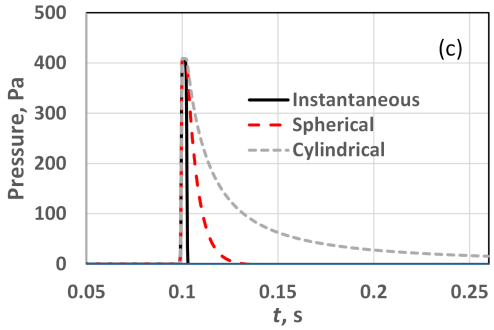

(c) Pressure just upstream of exit

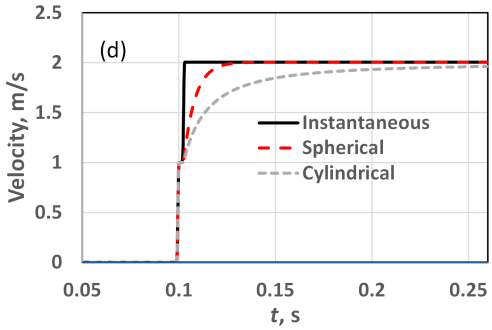

(d) Velocity just upstream of exit

Figure 9: Incident and reflected wavefronts inside the duct

section and spherical radiation in an external domain with an inner radius of 1 m. The generic behaviours of the two radial cases are similar, but the absolute delays with the constrained geometry implied by cylindrical radiation are much greater than those for the spherical radiation.

Figures 9c & 9d show the same incident and reflected waves just upstream of the duct exit. Their shapes are almost identical to those further upstream, but the time interval between the incident and reflected waves is much shorter. These curves provide a useful starting point for understanding the nature of the disturbance that propagates into the external domain. The behaviour in that region is illustrated in Fig. 10. In the upper row of the figure, the external radiation is modelled as spherical and, in the lower one, it is modelled as cylindrical. Accordingly, pressures in the upper row are scaled by the radius r and those in the lower row are scaled by $r^{0.5}$. For the graphs corresponding to $r/a = 1$ (*i.e.* at the interface between the two domains), the values shown in the time axis are exactly consistent with those in Fig. 9 for the waves inside the duct. That is, the wavefront begins

to arrive at the interface ($r/a = 1$) at approximately $t = 0.1$ s. For the graphs corresponding to $r/a = 3$ and $r/a = 5$, the times are offset by $2a/c_0$ and $4a/c_0$ respectively to compensate for the times of travel between successive locations. The purpose, namely to highlight changes in shape as the wave propagates, is analogous to the use of retarded time in the lower rows of Figs. 4, 5 and 6. However, the term 'retarded time' is not used here because the physical location of the effective origin of radial propagation is not defined uniquely.

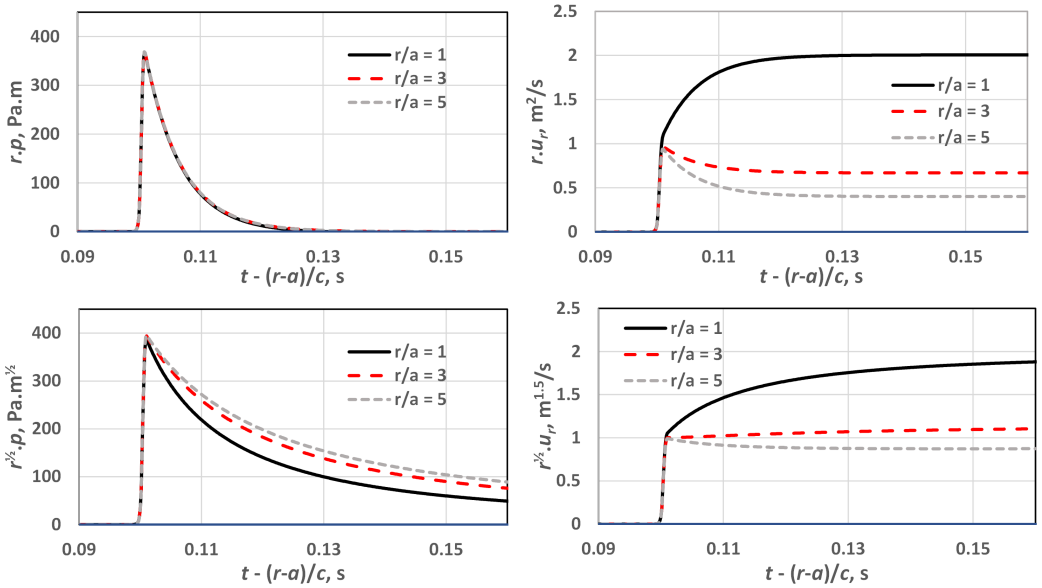

Figure 10: Spherical and cylindrical radiation of a pulse beyond a duct exit
Upper row: spherical radiation; lower row: cylindrical radiation

For both cases (spherical and cylindrical), the pressure behaves as a pulse with a steep initial rise and a gradual return towards ambient conditions That is, strong similarities exist between the external pulse and the conditions just upstream of the duct exit at the same offset time. It is also seen that for the cylindrical case, the scaled pressure histories have a close family resemblance with the corresponding decays presented in Fig. 5 for a B shaped line source. However, it is important to recognise that the B-shaped source was prescribed a priori whereas the pressure at the interface in the duct-exit case is a consequence of interactions between requirements in the internal and external domains. The most obvious demonstration of this difference is seen at $r = a$ during the periods of increasing pressure. In Fig. 6, the velocity decreases in tandem with the pressure whereas, in Fig. 10, it increases with decreasing pressure.

Qualitatively, the behaviour of the radiated signal is consistent with that highlighted above for N-shaped and B-shaped line sources. In particular, the initial sudden increase in pressure propagates almost in accordance with $p \cdot r^{0.5} =$ constant whereas the subsequent decaying portion of the source does not do so. One reason for this difference in behaviour is relatively straightforward and is described in Section 3.4 above. In all cases, the pressure at any particular radius and time is influenced by residual consequences of changes in velocity at the same radius at earlier times. In effect, it can be regarded as a weighted sum of these changes. Naturally, greater weighting factors will apply for recent changes than for less recent ones. As a consequence, the influence of past changes will be smaller during periods of rapid change than during less rapid ones.

The velocities in Fig. 10 are also scaled by r and $r^{0.5}$ for the spherical and cylindrical cases respectively. Again, the graphs for $r/a = 1$, 3 and 5 are almost coincident very close to the leading edge of the pulse, but differ strongly thereafter. However, although these graphs gradually approach asymptotic states, they do not decay to zero. Instead, they approach constant values that depend upon the radius. This is a consequence of the permanently sustained velocity of flow from the duct. As time increases, the extent of the region in which the mass flowrate is nearly equal to that at the duct exit also increases.

4.2. Comparison with CFD benchmark simulation

The coupled solution presented in Section 4.1 shows that the simple MoC methodology is able to model the influence of interactions between the two main flow fields. However, the abrupt change between planar and radial wave representations at the interface inevitably causes distortions close to the exit plane. Furthermore, the use of 1D representations of the domains prevents account being taken of spatial variations in pressure and velocity at the interface even though the simulated flow area is finite. Also, outside the duct, the stipulation of 1D symmetry disregards differences between waves travelling on rays in different directions – notably parallel to and normal to the x-axis. Accordingly, a detailed CFD simulation has been undertaken to provide guidance on the consequences of these limitations of the 1D methodology.

The CFD simulations have been undertaken using the software ANSYS Fluent v15.0 (ANSYS [17]). This could have been used with a spatially 2D coordinate system (x, y, t), but for in-house reasons related to generality, the authors chose to use (x, y, z, t) coordinates with boundary conditions that prevent variations in the z-direction (*i.e.* along the cylinder axis). This was done by stipulating zero velocity in the z-direction everywhere on the planes $z = \pm 4\Delta z$ and by checking

that all z-components of velocity in the solutions remained negligible. Nevertheless, to avoid confusion, the calculations are described as 2D in the following paragraphs, because the simulated wave propagation is 2D. A uniform square grid ($\Delta x = \Delta y = \Delta z = 0.05$ m) was used over the whole of the domain. The following options were used: density-based solver, Roe-FDS Flux Scheme, third-order MUSCL for spatial discretisation and second-order implicit time stepping for temporal discretisation. For the ambient speed of sound (approximately 340 m/s), the Courant-Friedrichs-Lewy (CFL) criterion for explicit numerical solutions of wave propagation in low Mach number flows requires that the numerical time step for a spatial grid length of 0.05 m must not exceed approximately 0.147 ms. However, the actual time step used was 0.05 ms even though the CFD integration is implicit. This is because extensive previous work by the authors has shown that this minimises the distortion of propagating waves. In addition to standard output facilities, user-defined functions were used to obtain maximum pressures automatically throughout the calculation domain.

In the following simulation, a steep wavefront propagates along a duct of rectangular cross-section and radiates into an external domain. The half-height of the duct shown in Fig. 11 is $R = 1$ m. In the actual 3D simulation, the total width of the duct is $8\Delta z$, as also is the width of the external domain beyond the exit. Physically, however, no variations occur in the z direction so the simulation is applicable to ducts of any width. This configuration is doubly symmetric in the $y-z$ plane so, in principle, it would be acceptable to simulate only one quarter of the overall flow domain (*i.e.* $y \geqslant 0$, $z \geqslant 0$). Nevertheless, to avoid any uncertainty, the full domain has been simulated in the solution presented below.

Inviscid conditions are prescribed in both methods of analysis (*i.e.* MoC & CFD) and free-slip is allowed along all solid surfaces (*i.e.* at $y = \pm R$ in the duct, on the face of the flange, and at $z = \pm 4\Delta z$ everywhere). In part, this is to avoid unnecessary complications in making comparisons, but it is also a good approximation to the true behaviour of waves in timescales that are much too small for vorticity diffusion to have a significant influence. Null-reflection boundary conditions exist at the outer limits of the external domain (depicted by broken lines in Fig. 11). More important, however, these boundaries are sufficiently far from the duct exit to ensure that any small reflections that could occur at them cannot reach locations at which solutions are presented during the overall period of the simulation.

A uniform, square grid ($\Delta x = \Delta y = \Delta z = 0.05$ m) has been used over the whole of the domain and no differences can be seen between the graphs presented herein and corresponding graphs obtained with a grid size of 0.1 m. Together with

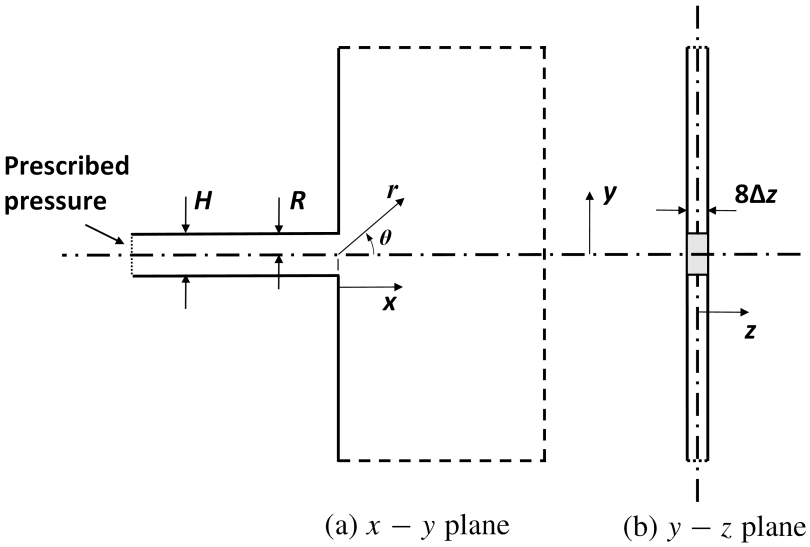

Figure 11: Geometry used in the CFD simulation – Not to scale
(NB: The highlighted region in (b) is the cross-section of the simulated duct)

the measures described in the preceding two paragraphs, this gives a high degree of confidence that the resulting solution of the underlying equations is a secure benchmark for assessing the strengths and limitations of the corresponding 1D MoC solutions.

The stagnation-pressure history shown in Fig. 12 is prescribed at the upstream end of the duct, causing a steep pressure wavefront to propagate towards the exit where it reflects and radiates. The prescribed wavefront causes a continuous increase in pressure from the ambient value to a new steady value. It is defined by an acceleration history that increases linearly to a maximum and then decreases linearly to zero. The durations of the increasing and decreasing periods are equal and, together with the fluid properties and prescribed ambient conditions, they determine the initial overall length of the wavefront. With the chosen acceleration history, the stagnation pressure increases by 2 kPa in a total of 50 ms, the maximum rate of change of pressure is 80 kPa/s and the overall length of the wavefront is $3.4\,H = 6.8\,R = 6.8$ m. Inertial effects cause the wavefront to shorten at a rate of approximately 6 m/s as it propagates along the duct. This effect is modelled in both the CFD and MoC simulations, but the overall shortening is small because the simulated length of duct is only 20 m and the wavefront travels at approximately 340 m/s.

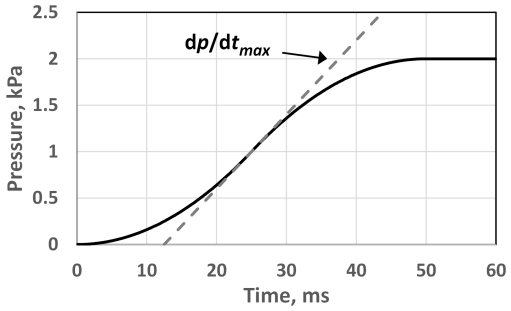

Figure 12: Prescribed stagnation pressure history at the upstream boundary

4.2.1. Reflected wavefront

Figure 13 compares CFD and MoC solutions of pressure and velocity histories at the mid-length of the duct. The wavefront caused by the imposed pressure history at the upstream boundary traverses this location during approximately $0.0294\,\text{s} < t < 0.0794\,\text{s}$. There is then a short period of nominally constant conditions until the reflection of the wavefront from the duct exit begins to arrive at approximately 0.0882 s. Thereafter, the pressure change decays towards zero and the velocity increases towards an asymptotic value of approximately 9.59 m/s. Both solutions are numerical and so both are subject to potential error. Nevertheless, it is reasonable to expect that the CFD solution will be the more accurate of the two because it has two key advantages. First, it represents the solid geometry correctly. Second, it imposes no non-physical constraints on directions of flow and wave propagation in either domain. Thus, it inherently allows for differences in the responses to high and low frequency components of incident wavefronts that give rise to circumferential variations discussed below. Accordingly, for present purposes, the CFD solution is treated as a benchmark and the differences in Fig. 13 are regarded as an indication that the MoC solution slightly underestimates the true delay times. Nevertheless, the differences between the two outcomes are sufficiently small to infer that, inside the duct, the coupled 1D MoC method of solution will be sufficiently accurate for many purposes, notably including practical engineering design.

4.2.2. Radiated waves

Figure 14 shows MoC and CFD solutions of pressure histories along three rays outside the duct, namely at 0°, 45° and 90° to the duct axis. The 1D MoC analysis does not distinguish between these directions so the values shown for it in the three boxes are identical. In the CFD geometry, all of the rays are deemed

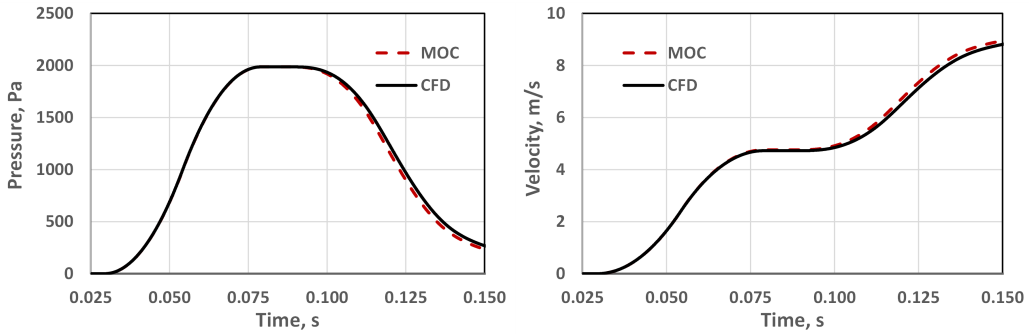

Figure 13: Incident and reflected wavefronts at the mid-length of the duct

to have a common origin at the centroid of the exit plane, but the interpretation of radial distances along them depends strongly on direction. For example, along the ray $\theta = 90°$ in Fig. 11a, the position $r/R = 1$ is at the outer edge of the exit plane, namely $x = 0$, $y = 1$. In contrast, along the ray $\theta = 0°$, it is 1 m beyond the exit plane, namely $x = 1$, $y = 0$. For the ray $\theta = 45°$ ray, it corresponds to $x = y = R/\sqrt{2}$.

Because the MoC solution is independent of θ, its curves in Fig. 14 can be used as a reference to enable use of the CFD solutions to assess differences along the three rays. It is seen that, at $r/R = 1$, the simulated pressure during approximately $t < 0.1$ s is greater along the 90° ray than along the 0° ray, but that the opposite is true at larger times. Similar behaviour exists at $r/R = 3$ and 5, but it is much less pronounced.

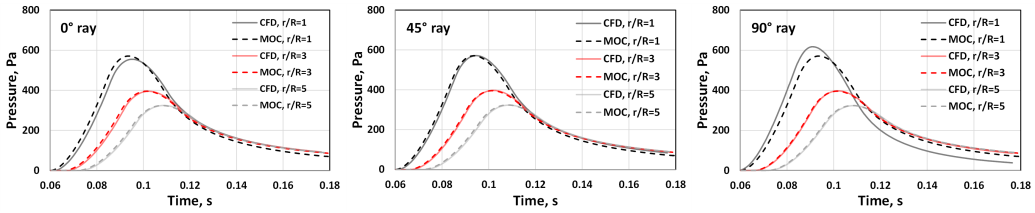

(a) 0° ray (b) 45° ray (c) 90° ray

Figure 14: Comparison of MoC and CFD pressure histories in the external domain

Next, consider the MoC solution itself and, for this purpose, assume that the CFD solution is close to 'true' values. In this case, the MoC pressures are closely realistic along the 45° ray, and the errors along the other two rays have opposite signs. This suggests the possibility that the MoC solution may be interpreted, at least approximately, as an average of values in all directions. The validity of this

interpretation is supported by Fig. 15, which compares mass flowrate histories through the exit plane for the two solutions.

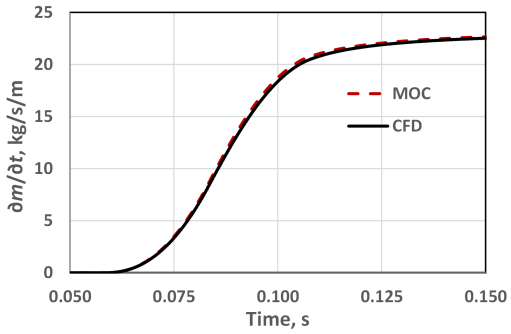

Figure 15: Mass flowrate histories in the duct exit plane

Useful deductions can also be made from comparisons of maximum pressures at successive locations along the various rays. Three columns in Table 1 show CFD solutions of values along the 0°, 45° and 90° rays. It is seen that the differences between these reduce with increasing distance from the origin (at the centroid of the exit plane in the CFD solution). In the near field, the pressure at any particular distance along the 0° ray is smaller than that on the 90° ray for the geometrical reason given above. At larger distances, however, the opposite trend exists, albeit only weakly in the simulated region. This is consistent with the well-known directional dependence in the far field for ducts radiating into 3D external domains. In practice, the directional dependence for radiation from unflanged ducts (not simulated herein) is even stronger. For completeness, it is declared that the use of 5 digit precision in the Table is not intended as a claim to 5 digit accuracy. Its purpose is to enable guidance to be inferred about the reducing dependence on θ as r/R increases.

The right-hand two columns in the Table compare averages of CFD values along five rays (0°, 22.5°, 45°, 67.5° & 90°) with the values from the MoC solution, and it is seen that there is close agreement between these. This is interpreted as further evidence that the simple 1D approximation of the whole flow-field captures the overall behaviour satisfactorily except in the inner region of the near-field.

The values listed in Table 1 have also been used to assess the reliability of the approximate relationship $p \cdot r^{0.5} =$ constant, or more strictly, to assess $p_{\max} \cdot r^{0.5} =$ constant, which should be approached in the far field, close to the leading edge of the pulse. This relationship is depicted in Fig. 16 by the continuous line labelled

	0° ray	45° ray	90° ray	Average of five rays (CFD)	MoC
$r/R = 0$	746.70	746.70	746.70	746.70	n/a
$r/R = 1$	554.74	571.41	617.43	579.25	579.54
$r/R = 2$	454.76	459.87	463.72	458.85	463.54
$r/R = 3$	394.91	397.07	396.91	395.62	399.98
$r/R = 4$	354.21	352.92	354.19	353.78	357.88
$r/R = 5$	324.19	323.10	323.39	323.82	327.16
$r/R = 6$	300.83	299.95	299.71	300.10	303.39
$r/R = 7$	281.96	281.26	280.72	281.42	284.26
$r/R = 8$	266.30	265.74	265.02	265.59	268.40

Table 1: Maximum pressures (Pa) along rays

$p^*_{\max} \cdot (r^*/r)^{0.5}$. The asterisk denotes a suitably large radius at which a reference value of $p_{\max} \cdot r^{0.5}$ has been evaluated, namely at $r/R = 8$ in this instance. By inspection, the pressure implied by this relationship tends to infinity as the radius tends to zero, and this is an inevitable consequence of focussing on rays with an origin at a single point, namely the centroid of the duct exit plane. In practice, of course, radiation occurs from all points in the plane, not only from its centroid.

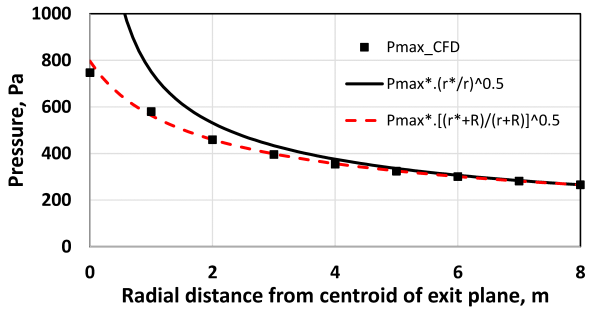

Figure 16: Comparison of $p^*_{\max} \cdot (r^*/r)^{0.5}$ and $p^*_{\max} \cdot ((r^* + R)/(r + R))^{0.5}$.

It has been found that a more accurate representation of the true behaviour can be obtained by making a small modification to the above formula, namely assuming $p_{\max} \cdot (r + \Delta r)^{0.5} = \text{constant}$, where Δr has a role that is loosely analogous to that of end-corrections in studies of reflected waves *inside* a duct. In

both cases, the purpose is to provide a reasonable representation of the influences of apparent delays in the observed behaviour. At large radii – *i.e.* in the far field – $(\Delta r)/r$ tends to zero so the two formulae are asymptotic to each another, but at small radii, they differ strongly. The broken line in Fig. 16 shows the particular case with $\Delta r = R$ together with averaged values along the rays $\theta = 0°$, 22.5°, 45°, 67.5° and 90° listed in Table 1 for the CFD solution. The correlation at radii exceeding approximately $2R$ (*i.e.* the cross-sectional dimension of the duct) is very close and it remains fairly close even at smaller radii where near-field conditions are dominant. That is, the expression

$$p_{\max}\left(1 + \frac{r}{R}\right)^{0.5} = \text{constant} \tag{17}$$

is a reasonable approximation to the actual behaviour averaged over the circumference of an arc of radius r. For completeness, it is emphasised that this correlation is only approximate and, of course, it has been inferred empirically, not analytically. In common with end corrections for internal reflections, the optimum value of Δr will depend on the frequency distribution in the incident wavefront.

5. Summary of Conclusions

Equations describing cylindrically-radial wave propagation have been developed into a form that enables their solution by the Method of Characteristics (MoC). In contrast with uniaxial (planar) or spherically-radial geometry, cylindrical wave propagation is dispersive and, although the qualitative behaviour is understood, no general analytical solutions exist. However, the numerical method has been validated by comparisons with analytical solutions for a special class of cases that has recently been found to be tractable. It has been shown that the physical dispersive behaviour is reproduced by the MoC analysis without evidence of strong additional dispersion due to numerical inaccuracies. Pressures close to the fronts of radiated pulses scale approximately with $r^{-0.5}$, but this correlation weakens rapidly with increasing distance behind the fronts. This contrasts with spherical radiation, for which pulse amplitudes scale with r^{-1} regardless of the distance behind their fronts. The development of the long tails behind cylindrically-radiating waves has been shown to follow a convolution-like behaviour.

The cylindrical MoC method has been coupled to a conventional planar MoC method at an interface that ensures continuity of area, flowrate and pressure even though the geometry changes discontinuously from uniaxial to radial. The coupled analysis has been used to simulate the reflection and radiation process after

a steep, planar wavefront arrives at a flanged duct exit. Although the incident wavefront causes a rapid change in pressure, its reflection is a gradual process that persists much longer than the corresponding delay in the case of spherical external radiation. This behaviour is necessarily also seen in the pulse that radiates into the external domain. The pulse is characterised by a rapid increase in pressure followed by a long decay. Its pressure amplitude at any radius during the rapid increase corresponds quite closely to an $r^{-0.5}$ scaling, but the amplitude during the subsequent decay period does not do so.

A coupled MoC solution has been compared with the corresponding solution using a 3D CFD package, thereby enabling zones of approximate validity of the MoC method to be assessed. The CFD analysis has confirmed the well-known behaviour that radiation varies with the azimuthal direction, being stronger in the direction of the duct axis than in other directions. However, it has also shown that the MoC solution approximates closely to averages of values obtained for rays in all azimuthal directions.

In the coupled, 1D MoC analysis, the interface between the planar and radial approximations is abrupt and is deemed to be at a radius that ensures a flow area equal to the cross-sectional area of the planar region. In contrast, for the CFD analysis, the transition between these regions is not abrupt, but variations in pressure along individual rays nevertheless behave similarly to those in the MoC analysis. It has been found that pressure amplitudes close to the leading edge of a steeply-rising pulse radiating from a duct of uniform width can be represented more closely by $p_{\max} \cdot (r + \Delta r)^{0.5} = \text{constant}$ than by $p_{\max} \cdot r^{0.5} = \text{constant}$, where r is measured from the centroid of the exit plane and Δr is a small distance inside the duct. In the case of a duct with a flanged exit, Δr is approximately equal to the half-height of the duct. In effect, this adjustment is analogous to the end-correction used when considering internal reflections of plane waves at duct exits.

6. Acknowledgement

The third author is pleased to acknowledge financial support from the Sichuan Science and Technology Program [grant number 2021YFG0214].

Appendix A. An analytic test solution

Appendix A.1. Introduction

In this appendix we present the analytic test solution used in Section 3 above. It is an abridged version of the solution given in [2], with sufficient details to ease

a direct comparison.

Appendix A.2. The problem

We construct the fields of pressure fluctuation $p - p_0$ and velocity $\boldsymbol{v}$ produced by a line source (the time derivative of a uniform mass source, concentrated in the z-axis) with time dependent amplitude q that is switched on at $t = 0$. The source is small enough to justify linearisation. From symmetry it can be immediately inferred that (i) there is no z dependence in the problem, so it is effectively 2D, and (ii) the only nonzero component of velocity $\boldsymbol{v}$ is its radial component v. The field is described by the linearised conservation equations, recast into the standard 2D inhomogeneous wave equation

$$\frac{1}{c_0^2}\frac{\partial^2 p}{\partial t^2} - \nabla^2 p = \delta(\boldsymbol{x})q, \quad \rho_0\frac{\partial v}{\partial t} = -\frac{\partial p}{\partial r}, \tag{A.1}$$

where $\delta(\boldsymbol{x})$ denotes the delta-function, $\boldsymbol{x} = (x, y) = (r\cos\vartheta, r\sin\vartheta)$, and ρ_0, p_0, and c_0 are the ambient density, pressure and sound speed, respectively. The radial mass flowrate (per unit source length) at distance r and time t is given by $\dot{m}(r, t) = 2\pi\rho_0 r\, v(r, t)$. The source mass flowrate is then $\dot{m}(0, t)$ and satisfies $\frac{\partial}{\partial t}\dot{m}(0, t) = q(t)$.

We assume a reference time scale b, induced by source $q(t)$. (For example a pulse width or a typical oscillation time.) The smallness of the source will be brought about by a small dimensionless amplitude A. We make dimensionless and rescale as follows (for notational convenience we leave most of the symbols the same): $t := bt$, $\boldsymbol{x} := c_0 b\,\boldsymbol{x}$, $p := p_0 + \rho_0 c_0^2 A p$, $v := c_0 A v$, $\dot{m} := \rho_0 c_0^2 b A \Phi$, $q := \rho_0 c_0^2 A q$, to obtain

$$\frac{\partial^2 p}{\partial t^2} - \nabla^2 p = \delta(\boldsymbol{x})q(t), \ \frac{\partial v}{\partial t} = -\frac{\partial p}{\partial r}, \ \Phi = 2\pi r v, \ \frac{\partial}{\partial t}\Phi(0, t) = q. \tag{A.2}$$

From the standard Green's function [5, p. 156], [6, App. E] and some rewriting, we obtain the solution [3, Art. 302], [7, p. 219]

$$p(r, t) = \frac{1}{2\pi}H(\zeta - 1)\int_0^{\operatorname{acosh}\zeta} q(t - r\cosh\theta)\,\mathrm{d}\theta \tag{A.3}$$

$$v(r, t) = \frac{1}{2\pi}H(\zeta - 1)\int_0^{\operatorname{acosh}\zeta} q(t - r\cosh\theta)\cosh\theta\,\mathrm{d}\theta \tag{A.4}$$

where H is the Heaviside unit step-function, and

$$\zeta = \frac{t}{r}, \quad \operatorname{acosh} x = \log\bigl(x + \sqrt{x^2 - 1}\bigr).$$

The velocity v includes an integration "constant" (a function of r) that has to be determined from continuity arguments in $t = r$ (*i.e.* $\zeta = 1$). For smooth and finite q, $v = 0$ at $\zeta = 1$ and the constant is zero.

For analytically exact solutions, we need for q a well chosen class of functions such that their primitives can be found with $\cosh\theta$ in the argument. Suitable candidates are polynomials, because integral powers of $\cosh\theta$ are primitivable.

Appendix A.3. Simple powers

Consider the source shape function

$$f_n(t) = H(t)t^n.$$

For a source $q(t) = f_n(t)$ we find from (A.3) and (A.4) a set of elementary solutions

$$p(r,t) = \frac{1}{2\pi} H(\zeta - 1) r^n P_n(\zeta), \quad v(r,t) = \frac{1}{2\pi} H(\zeta - 1) r^n V_n(\zeta), \tag{A.5}$$

with

$$P_n(\zeta) = \int_0^{\operatorname{acosh}\zeta} (\zeta - \cosh\theta)^n \,\mathrm{d}\theta, \;\; V_n(\zeta) = \int_0^{\operatorname{acosh}\zeta} (\zeta - \cosh\theta)^n \cosh\theta \,\mathrm{d}\theta \tag{A.6}$$

We find for the first few orders

$$\begin{aligned}
P_0(\zeta) &= \operatorname{acosh}\zeta \\
P_1(\zeta) &= \zeta \operatorname{acosh}\zeta - \sqrt{\zeta^2 - 1} \\
P_2(\zeta) &= (\zeta^2 + \tfrac{1}{2}) \operatorname{acosh}\zeta - \tfrac{3}{2}\zeta \sqrt{\zeta^2 - 1} \\
P_3(\zeta) &= (\zeta^3 + \tfrac{3}{2}\zeta) \operatorname{acosh}\zeta - (\tfrac{11}{6}\zeta^2 + \tfrac{2}{3}) \sqrt{\zeta^2 - 1} \\
P_4(\zeta) &= (\zeta^4 + 3\zeta^2 + \tfrac{3}{8}) \operatorname{acosh}\zeta - (\tfrac{25}{12}\zeta^3 + \tfrac{55}{24}\zeta) \sqrt{\zeta^2 - 1} \\
P_5(\zeta) &= (\zeta^5 + 5\zeta^3 + \tfrac{15}{8}\zeta) \operatorname{acosh}\zeta - (\tfrac{137}{60}\zeta^4 + \tfrac{607}{120}\zeta^2 + \tfrac{8}{15}) \sqrt{\zeta^2 - 1} \\
P_6(\zeta) &= (\zeta^6 + \tfrac{15}{2}\zeta^4 + \tfrac{45}{8}\zeta^2 + \tfrac{5}{16}) \operatorname{acosh}\zeta - (\tfrac{49}{20}\zeta^5 + \tfrac{91}{10}\zeta^3 + \tfrac{231}{80}\zeta) \sqrt{\zeta^2 - 1}
\end{aligned} \tag{A.7}$$

$$
\begin{aligned}
V_0(\zeta) &= & & & & \sqrt{\zeta^2-1}\\
V_1(\zeta) &= & & -\tfrac{1}{2}\ \operatorname{acosh}\zeta & & +\tfrac{1}{2}\zeta\sqrt{\zeta^2-1}\\
V_2(\zeta) &= & & -\zeta\ \operatorname{acosh}\zeta & & +(\tfrac{1}{3}\zeta^2+\tfrac{2}{3})\sqrt{\zeta^2-1}\\
V_3(\zeta) &= & & -(\tfrac{3}{2}\zeta^2+\tfrac{3}{8})\ \operatorname{acosh}\zeta & & +(\tfrac{1}{4}\zeta^3+\tfrac{13}{8}\zeta)\sqrt{\zeta^2-1}\\
V_4(\zeta) &= & & -(2\zeta^3+\tfrac{3}{2}\zeta)\ \operatorname{acosh}\zeta & & +(\tfrac{1}{5}\zeta^4+\tfrac{83}{30}\zeta^2+\tfrac{8}{15})\sqrt{\zeta^2-1}\\
V_5(\zeta) &= & -(\tfrac{5}{2}\zeta^4+\tfrac{15}{4}\zeta^2+\tfrac{5}{16})\ \operatorname{acosh}\zeta & & +(\tfrac{1}{6}\zeta^5+\tfrac{97}{24}\zeta^3+\tfrac{113}{48}\zeta)\sqrt{\zeta^2-1}\\
V_6(\zeta) &= -(3\zeta^5+\tfrac{15}{2}\zeta^3+\tfrac{15}{8}\zeta)\ \operatorname{acosh}\zeta & & +(\tfrac{1}{7}\zeta^6+\tfrac{759}{140}\zeta^4+\tfrac{1779}{280}\zeta^2+\tfrac{16}{35})\sqrt{\zeta^2-1}
\end{aligned}
\tag{A.8}
$$

Appendix A.4. Combinations

A wide class of solutions can be constructed from these elementary solutions by linear combinations of powers of different orders and delays. In particular, we can construct the solution for sources of finite duration, *i.e.* pulses, by subtracting a delayed version of itself, re-expanded in the delayed variable $t-1$. Note that the dimensionless pulse duration is equal to unity because we use throughout this analysis the dimensional duration as our reference time (*viz. b*). We have then sources like

$$H(t)g(t) - H(t-1)\tilde{g}(t-1), \tag{A.9}$$

where $g(t)$ is a polynomial in t of any degree, and $\tilde{g}(t-1)$ is identically equal to $g(t)$ but re-expanded into a polynomial in $t-1$ of the same degree. (This is always possible.) We will consider here two types of pulses, parametrised by integer n for a varying smoothness in $t=0$ and $t=1$: the *bulge-shaped* function $q(t)=B_n(t)$ of order $n \geqslant 0$

$$B_n(t) = 4^n(H(t)-H(t-1))t^n(1-t)^n, \tag{A.10}$$

and the *N-shaped* function $q(t)=N_n(t)$ of order $n \geqslant 1$

$$
\begin{aligned}
N_n(t) &= (2n-1)^{\frac{1}{2}}\Big(\frac{4n-2}{n-1}\Big)^{n-1}(H(t)-H(t-1))(1-2t)t^{n-1}(1-t)^{n-1},\\
N_1(t) &= H(t)(1-2t)+H(t-1)(1+2(t-1)).
\end{aligned}
\tag{A.11}
$$

All B_n and N_n are normalised such that their maximum is unity. To construct the solutions p and v, the coefficients of $H(t)$ and $H(t-1)$ have to be expanded

as polynomials in t and $t-1$, respectively. Explicitly, and with the short-hand notation $t_- = t-1$, we have for the first few orders:

$$
\begin{aligned}
B_0(t) &= H(t) - H(t_-) \\
B_1(t) &= -4H(t)(t^2 - t) + 4H(t_-)(t_-^2 + t_-) \\
N_1(t) &= -H(t)(2t-1) + H(t_-)(2t_- + 1) \\
B_2(t) &= 16H(t)(t^4 - 2t^3 + t^2) - 16H(t_-)(t_-^4 + 2t_-^3 + t_-^2) \\
N_2(t) &= 6\sqrt{3}H(t)(2t^3 - 3t^2 + t) - 6\sqrt{3}H(t_-)(2t_-^3 + 3t_-^2 + t_-) \\
B_3(t) &= -64H(t)(t^6 - 3t^5 + 3t^4 - t^3) + 64H(t_-)(t_-^6 + 3t_-^5 + 3t_-^4 + t_-^3) \\
N_3(t) &= -25\sqrt{5}H(t)(2t^5 - 5t^4 + 4t^3 - t^2) + 25\sqrt{5}H(t_-)(2t_-^5 + 5t_-^4 + 4t_-^3 + t_-^2)
\end{aligned}
\tag{A.12}
$$

Appendix A.5. Return to dimensional form

Eventually, the required solution is found by selecting the terms of the type $H(t)t^n$ and $H(t_-)t_-^n$ in the above source considered, finding the corresponding solutions (A.5), and combining them accordingly in dimensional form. To illustrate the methodology, one may consider the example of the source of shape N_1, for which we obtain dimensionally

$$
q(t) = \rho_0 c_0^2 A\left[-H(t)\left(2\frac{t}{b} - 1\right) + H(t-b)\left(2\left(\frac{t}{b} - 1\right) + 1\right)\right], \tag{A.13}
$$

$$
\begin{aligned}
v(r,t) = c_0 A \frac{1}{2\pi}\Bigg[&-H\left(t - \frac{r}{c_0}\right)\left(2\frac{r}{c_0 b}V_1\left(\frac{c_0 t}{r}\right) - V_0\left(\frac{c_0 t}{r}\right)\right) \\
&+ H\left(t - b - \frac{r}{c_0}\right)\left(2\frac{r}{c_0 b}V_1\left(c_0\frac{t-b}{r}\right) + V_0\left(c_0\frac{t-b}{r}\right)\right)\Bigg],
\end{aligned} \tag{A.14}
$$

$$
\begin{aligned}
p(r,t) = p_0 + \rho_0 c_0^2 A \frac{1}{2\pi}\Bigg[&-H\left(t - \frac{r}{c_0}\right)\left(2\frac{r}{c_0 b}P_1\left(\frac{c_0 t}{r}\right) - P_0\left(\frac{c_0 t}{r}\right)\right) \\
&+ H\left(t - b - \frac{r}{c_0}\right)\left(2\frac{r}{c_0 b}P_1\left(c_0\frac{t-b}{r}\right) + P_0\left(c_0\frac{t-b}{r}\right)\right)\Bigg].
\end{aligned} \tag{A.15}
$$

Using v, it follows that $\dot{m} = 2\pi\rho_0 r v$. The hyperbolicity of the wave equation (A.1) (no information travels back in time) together with the infinite domain (hence only outward radiating waves) makes it possible to mimic the field of a fictitious vibrating cylindrical surface positioned at (dimensional) radius $r = a$.

For this, we take the velocity $v(a, t \geqslant a/c_0)$ to find the boundary condition at $r = a$, either directly, or as the linearised fluctuating position

$$r = a + \int_{a/c_0}^{t} v(a, \tau)\, \mathrm{d}\tau. \tag{A.16}$$

Then the corresponding $p(r, t)$ and $v(r, t)$ describe the field produced by the surface in domain $r > a$.

References

[1] N.L. Balazs, Wave propagation in even and odd dimensional spaces, Proc. Phys. Soc. A 68, 1955, pp. 521.

[2] S.W. Rienstra, A class of cylindrically symmetric exact solutions of the wave equation, J. Sound Vib. 545, 2023, 117430.

[3] H. Lamb, Hydrodynamics, Dover Publications, New York, 1945. [An unabridged and unaltered republication of the 6th (1932) edition of the work originally published in 1879].

[4] D.S. Jones, Acoustic and Electromagnetic Waves, Clarendon Press, Oxford, 1986.

[5] N. Bleistein, Mathematical Models for Wave Phenomena, Academic Press, Inc., London, 1984.

[6] S.W. Rienstra, A. Hirschberg, An Introduction to Acoustics, Technical University of Eindhoven. Extended and revised edition of IWDE 92-06, 2004, Available at: http://www.win.tue.nl/∼sjoerdr/papers/boek.pdf . Google Scholar

[7] G.B. Whitham, Linear and Nonlinear Waves, Wiley, New York, 1974.

[8] M.J. Lighthill, Waves in Fluids, Cambridge University Press, 1978.

[9] A.E. Vardy, A.S. Tijsseling, Method of characteristics for transient, spherical flows, Appl. Math. Model., 77, 2020, pp. 810-828.

[10] J.A. Owczarek, Fundamentals of Gas Dynamics, International Textbook Co., Scranton, PA, 1964.

[11] A. Kluwick, The analytical method of characteristics, Progr. Aerospace Sc., 19, 1981, pp. 197-313.

[12] X. Li, C. Zhang, X. Wang, X. Hu, Numerical study of underwater shock wave by a modified method of characteristics, J. App. Phys. 115, 2014, 104905.

[13] C. Zhang, X. Li, C. Yang, A modified method of characteristics and its application in forward and inversion simulations of underwater explosion, AIP Advances, 6 (7), 2016, 075319.

[14] H. Steine, W. Gretler, The propagation of spherical and cylindrical shock waves in real gases, Phys Fluids, 6 (6), 1994, pp. 2154-2164.

[15] A.N. Kraiko, Rapid cylindrically and spherically symmetric strong compression of a perfect gas, J. App. Maths & Mech, 71 (5), 2007, pp. 676-689.

[16] H. Wang, A.E. Vardy, H. Bi, Characteristics of pressure waves radiated from tunnel portals in cuttings, J. Sound Vib., 521, 2022, 116664.

[17] ANSYS FLUENT. User Manual, Release 15.0, 2014.